# Discovering and Characterising Exoplanets and Ultracool Dwarfs with the Square Kilometre Array

Robert D. Kavanagh,[1,2] Juan B. Climent,[3] Philippe Zarka,[4,5] Joseph R. Callingham,[2,1] Yuka Fujii,[6,7] Corentin K. Louis,[4] Laurent Lamy,[8,4,5] Mayank Narang,[9] J. Sebastian Pineda,[10] Harish K. Vedantham,[2,11] Sanne Bloot,[2,11] Jean-Mathias Grießmeier,[12,5] Jose Carlos Guirado,[3,13] Simranpreet Kaur,[14,15] T. Joseph W. Lazio,[9] Miguel Pérez-Torres[16] and Alice Zurlo[17,18]

[1]*Anton Pannekoek Institute for Astronomy, University of Amsterdam, 1098 XH Amsterdam, The Netherlands*
[2]*ASTRON, The Netherlands Institute for Radio Astronomy, Oude Hoogeveensedijk 4, 7991 PD Dwingeloo, The Netherlands*
[3]*Departament d'Astronomia i Astrofísica, Universitat de València, C. Dr. Moliner 50, E-46100 Burjassot, València, Spain*
[4]*LIRA, Observatoire de Paris, Université PSL, Sorbonne Université, Université Paris Cité, CY Cergy Paris Université, CNRS, 92190 Meudon, France*
[5]*Observatoire Radioastronomique de Nançay, Observatoire de Paris, CNRS, PSL, Univ. Orléans, Nançay, France*
[6]*National Astronomical Observatory of Japan, 2–21–1 Osawa, Mitaka, Tokyo 181–8588, Japan*
[7]*Department of Earth and Planetary Science, University of Tokyo, 7-3-1 Hongo, Bunkyo-ku, Tokyo 113-0033, Japan*
[8]*Aix Marseille Université, CNRS, CNES, LAM, Marseille, France*
[9]*Jet Propulsion Laboratory, California Institute of Technology, Pasadena, CA 91109, USA*
[10]*University of Colorado Boulder, Laboratory for Atmospheric and Space Physics, 3665 Discovery Drive, Boulder CO, 80303, USA*
[11]*Kapteyn Astronomical Institute, University of Groningen, Landleven 12, 9747 AD Groningen, Netherlands*
[12]*LPC2E, OSUC, Univ Orleans, CNRS, CNES, Observatoire de Paris, F-45071 Orleans, France*
[13]*Observatori Astronòmic, Universitat de València, Parc Científic, C. Catedrático José Beltrán 2, E-46980 Paterna, València, Spain*
[14]*Institut de Ciències de l'Espai (ICE-CSIC), Campus UAB, Carrer de Can Magrans s/n, 08193 Cerdanyola del Vallès, Catalonia, Spain*
[15]*Institut d'Estudis Espacials de Catalunya (IEEC), 08860 Castelldefels, Barcelona, Catalonia, Spain*
[16]*Instituto de Astrofísica de Andalucía (IAA-CSIC), Glorieta de la Astronomía s/n, E-18008 Granada, Spain*
[17]*Instituto de Estudios Astrofísicos, Facultad de Ingeniería y Ciencias, Universidad Diego Portales, Av. Ejército Libertador 441, Santiago, Chile*
[18]*Millennium Nucleus on Young Exoplanets and their Moons (YEMS)*

E-mail: r.d.kavanagh@uva.nl

 

The majority of the Solar System planets are sources of bright radio emission, driven by energetic electrons trapped within each planet's magnetic field. Detection of this emission from exoplanets provides a unique opportunity to characterise their magnetic fields, which is key to determining the atmospheric evolution of exoplanets. However, a conclusive detection of radio emission from an exoplanet remains at large, primarily due to a lack of sensitivity at low radio frequencies. On the other hand, planet-like radio signatures have been detected on objects called ultracool dwarfs (UCDs) for over two decades. UCDs are of comparable sizes to Jupiter, but are more massive. They also possess similar interior structures to Jupiter, the region where magnetic fields are generated. Therefore, UCDs are ideal targets to study to advance our understanding of how magnetic fields manifest at planetary scales. In this Chapter, we outline the revolutionary role that the Square Kilometre Array will play in the study of exoplanets and UCDs. We anticipate that it will facilitate the first detection of radio emission from giant exoplanets with strong magnetic fields, and will deliver thousands of detections of UCDs within a few hundred parsecs. Combined with very long baseline interferometry, we also expect that astrometric monitoring will enable the detection of planets of a few Earth masses orbiting nearby radio-emitting UCDs. These findings will open a new window into how planets form and evolve in extrasolar systems.

## 1 Introduction

Detecting and characterising planets in extrasolar systems, known as exoplanets, is key to understanding the diversity of planetary systems and placing our own Solar System in context. The demographics and atmospheric compositions of exoplanets inform us about their formation (Fulton and Petigura, 2018), evolution (Schlecker et al., 2022; Stefánsson et al., 2023), and potential habitability (Espinoza et al., 2025). While we have now discovered over 6 000 exoplanets, current detection methods heavily skew our statistics towards massive planets that orbit close to their host stars in edge-on configurations from our vantage point. Additionally, we currently lack the technology to directly detect the magnetic fields of exoplanets (Oklopčić et al., 2020; Ben-Jaffel et al., 2022), which is key to regulating planetary atmospheric escape (Owen and Adams, 2014; Dong et al., 2019; Carolan et al., 2021) and ultimately habitability in the case of terrestrial planets (Blackman and Tarduno, 2018).

Brown dwarfs and late M dwarfs (effective temperatures $\lesssim$ 2700 K), collectively known as ultracool dwarfs (UCDs), provide unique insights into the magnetic fields and atmospheres of exoplanets. With sizes comparable to Jupiter but masses about 13 to 70 times greater (Davis et al., 2025), thousands of UCDs have been discovered in our astronomical backyard[1]. The cool atmospheres of UCDs are excellent analogues for those of gas giant exoplanets, and can be studied in isolation from the irradiation of a host star (Vos et al., 2023; Faherty et al., 2024). UCD demographics also provide clues about how both stars and planets form (Palau et al., 2024). They also possess powerful magnetic fields that can be detected with current technology, which allow us to probe their interior structures. Since the structure, composition, and convective properties of UCD interiors are thought to resemble those of Jupiter (Showman et al., 2020), studying magnetism on UCDs provides insights into the magnetic field generation and interior structures of exoplanets, the latter of which are notoriously difficult to study (van Dijk and Miguel, 2025).

In this Chapter, we discuss the revolutionary role the Square Kilometre Array (SKA) will play in the detection and study of exoplanets and UCDs. This is anticipated for two reasons. First, bright low-frequency radio emission is associated with all magnetised planets in the Solar System (Zarka, 1998). Second, emission reminiscent of that observed on the Solar System planets is prevalent on UCDs. We expect that the unprecedented sensitivity of the SKA will deliver the first concrete detections of radio emission from magnetised giant planets, and will yield thousands of detections of UCDs within a few hundred parsecs from Earth. Additionally, long-term monitoring with the SKA in combination with very long baseline interferometry will enable astrometric detection of exoplanets orbiting radio-loud stars and UCDs. The wealth of new science enabled by the SKA will cement radio astronomy as a core technique for discovering and characterising exoplanets and UCDs in the coming decades.

[1] The UltracoolSheet: Photometry, Astrometry, Spectroscopy, and Multiplicity for 4000+ Ultracool Dwarfs and Imaged Exoplanets

## 2 Radio emission from planets in the Solar System

To appreciate the SKA's potential for discovering and characterising exoplanets and UCDs, we first provide an overview of radio emission from the planets in the Solar System. Most Solar System planets with intrinsic magnetic fields (Earth, Jupiter, Saturn, Uranus, Neptune) are sources of bright low-frequency radio emission (Zarka, 1998). This radio emission is particularly prevalent from Jupiter, which outshines the quiet Sun by up to three orders of magnitude at frequencies below 40 MHz (Zarka, 2007). Planetary radio emission is primarily driven by the electron cyclotron maser instability (Treumann, 2006). Jupiter is also a known source of broadband emission from $\sim$ 10 MHz to 10 GHz, which is generated via synchrotron processes (de Pater, 1981; Girard et al., 2016). We discuss the core physics underpinning these processes in Sections 2.1 and 2.2.

### 2.1 Auroral emission

Electron cyclotron maser (ECM) emission is driven by the amplification of electromagnetic waves by semi-relativistic (keV) electrons in strongly magnetised, low density plasmas. First proposed as the driving mechanism of the Earth's kilometric ($\sim$100 to 600 kHz) radio emission (Wu and Lee, 1979), ECM has been validated for the Earth, Jupiter, and Saturn from a wealth of in-situ observations (e.g Louarn et al., 1990; Lamy et al., 2010; Collet et al., 2024). Given its prevalence in the Solar System, ECM is thought to be widely applicable to magnetised exoplanets, as well as UCDs and stars given their similar plasma properties (Treumann, 2006; Zarka, 2007).

When electrons are accelerated in a planetary magnetic field, they travel towards the magnetic poles. If an electron's velocity vector is predominantly aligned with the magnetic field, it will precipitate into the atmosphere and collide with atmospheric molecules. These collisions can produce bright emission from infrared to X-ray wavelengths (Badman et al., 2015; Saur et al., 2021). Electrons that do not precipitate however, i.e. those with velocity vectors that are predominantly misaligned (perpendicular) to the magnetic field, can amplify electromagnetic waves close to the electron cyclotron frequency (Treumann, 2006; Collet et al., 2024):

$$\nu_{\rm c} = \frac{eB}{2\pi m_e} \approx 2.8 \times \frac{B}{1\ \rm Gauss}\ \rm MHz, \tag{1}$$

where $e$ and $m_e$ are the electron charge and mass, and $B$ is the local magnetic field strength. On the Earth, the optical signature of the precipitating electrons manifests as the well-known phenomenon of the aurora borealis and australis. Hence, this emission is generally referred to as 'auroral' emission, irrespective of wavelength. We adopt this terminology from here onwards.

Auroral radio emission is highly circularly/elliptically polarised (Zarka, 1998, 2004; Lamy, 2020; Zarka et al., 2021), and provides a direct way to constrain the field strengths of magnetised bodies (Equation 1). Jupiter exhibits the strongest magnetic field of all the Solar System planets. With a maximum strength of $\sim$ 14 G, its auroral emission extends up to $\sim$ 40 MHz (Zarka, 2007). A condition for radio aurorae to be generated is that the cyclotron frequency at the emission site exceeds the plasma frequency:

$$\nu_{\rm p} = \sqrt{\frac{e^2 n_e}{\pi m_e}} \approx 9 \times 10^{-3} \sqrt{\frac{n_e}{1\ \rm cm^{-3}}}\ \rm MHz, \tag{2}$$

where $n_e$ is the free electron density. In other words, detection of auroral emission also provides a constraint on the local electron density. Recent in-situ observations of Jupiter taken by *Juno* indicate that $\nu_\mathrm{c} \gtrsim 3\nu_\mathrm{p}$ in order for ECM emission to be generated (Collet et al., 2025).

Another defining characteristic of auroral radio emission is its beam pattern, which is highly anisotropic. Emission is beamed along the surface of a cone that is centered on the magnetic field line at the emission site, with an opening angle $\leq 90°$. This causes auroral radio emission to manifest as short pulses in time as the emission cone rotates in and out of view of the observer. This characteristic can be exploited to infer the geometry of the magnetic field at the source location (Lamy et al., 2008a; Kuznetsov et al., 2012; Louis et al., 2019; Bastian et al., 2022; Kavanagh et al., 2024).

Not long after *Voyager 1* discovered auroral radio emission on Saturn (Kaiser et al., 1980), Desch and Kaiser (1984) reported that the brightness of radio aurorae on the magnetised Solar System planets appear to be strongly correlated with the solar wind energy flux intercepted by each planet's magnetic field. Follow-up studies (e.g. Zarka et al., 2001; Zarka, 2007) interpreted this correlation as the intercepted solar wind energy regulating the energy released via magnetic reconnection in the nightside of the planet's magnetic field (Dungey, 1961), providing the source of the keV electrons necessary to power aurorae. By analysing data from all the Solar System planets and moons with intrinsic magnetic fields, Zarka et al. (2018) demonstrated that any magnetised body's auroral radio power scales linearly with the *magnetic* energy flux of the plasma flow it intercepts. This scaling law is often referred to as the radio-magnetic scaling law.

The magnetic power of the solar wind that is intercepted by a magnetised planet is (Zarka et al., 2018)

$$P_\mathrm{mag} = \frac{{B_\mathrm{w}}^2 \sin^2\theta}{\mu_0} \times \Delta u \times \pi {R_\mathrm{m}}^2, \tag{3}$$

where $B_\mathrm{w}$ is the magnetic field strength of the solar wind, $\mu_0$ is the vacuum permeability, and $\Delta u$ is the velocity of the solar wind relative to the orbital motion of the planet. $\theta$ is the angle between the direction of $B_\mathrm{w}$ and $\Delta u$, both of which are vectors in three dimensions. $R_\mathrm{m}$ is the size of 'magnetosphere' (Bagenal, 2013), the region where the planet's magnetic pressure dominates. This can be estimated by balancing the magnetic pressure of the planet with the total pressure of the incident solar wind $p_\mathrm{w}$. If the planetary magnetic field is dipolar and with its axis perpendicular to the inflowing wind, one can show that (Voigt, 1995; Grießmeier et al., 2004)

$$\frac{R_\mathrm{m}}{R_\mathrm{p}} = \left(\frac{f_0 {B_\mathrm{p}}^2}{4\mu_0 p_\mathrm{w}}\right)^{1/6} \tag{4}$$

where $R_\mathrm{p}$ is the planetary radius, $B_\mathrm{p}$ is the planetary magnetic field strength at its magnetic poles, and $f_0$ is the magnetopause form factor. For a realistic magnetosphere with a magnetotail, $f_0 = 1.16$ (Voigt, 1995). Equation 3 can be thought of as the flow of Poynting flux through the magnetospheric cross-sectional area $\pi {R_\mathrm{m}}^2$ at a flow velocity of $\Delta u$. In the Solar System, $\sim 0.2\%$ of the magnetic energy flux intercepted by each planet's magnetosphere is estimated to be converted into radio emission (Zarka, 2025).

There are also additional drivers of aurorae on some of the magnetised Solar System planets. For instance, Jupiter is known to magnetically interact with its innermost moons through 'sub-Alfvénic' interactions (Zarka, 2007; Saur et al., 2013), which accelerate electrons from the surrounding plasma environment. These electrons accelerate along the planet-moon flux tube, powering auroral ECM emission as described above. The point where the surrounding plasma ceases to rigidly co-rotate with Jupiter is also thought to be a source of electron acceleration that can drive the generation of aurorae (Hill, 2001; Cowley and Bunce, 2001). We note however that the role this mechanism plays in driving auroral emission has been disputed (see Bonfond et al., 2020; Yao et al., 2022; Sicorello et al., 2025).

### 2.2 Radiation belt emission

The magnetospheres of the Earth, Jupiter, Saturn, Uranus, Neptune and Ganymede are also known to trap energetic charged particles in regions near their magnetic equators, known as radiation belts (Mauk and Fox, 2010; Kollmann et al., 2022). The kinetic energies of these particles are measured to range from $\sim 10$ keV to tens of MeV. Electrons in this energy regime can power broadband radio emission via (gyro)synchrotron processes. This emission is brightest close to the critical frequency (Longair, 2011):

$$\nu_{\rm crit} = \frac{3}{2}\gamma^2 \nu_{\rm c} \sin\alpha, \tag{5}$$

where $\gamma$ is the Lorentz factor and $\alpha$ is the angle between the magnetic field and the electron's velocity vector.

As synchrotron emission is an incoherent emission process, it does not produce the same brightness levels achieved by the coherent ECM mechanism. Nevertheless, the high energy electrons trapped within Jupiter's magnetosphere produce synchrotron emission that has been detected from $\sim 10$ MHz to 10 GHz (Bolton et al., 2002; Girard et al., 2016). This emission is at least 5 orders of magnitude dimmer than Jupiter's auroral emission (Girard et al., 2016), and exhibits significant linear polarisation (Bolton et al., 2002) – a characteristic trait of synchrotron emission (Rybicki and Lightman, 1986). The emission pattern of synchrotron emission is also highly collimated, which induces rotational modulation in Jupiter's radiation belt emission (Velusamy et al., 2020; Matuszewska et al., 2022).

While trapped energetic particles have also been measured in-situ for the Earth, Saturn, Uranus, Neptune, and Ganymede (Mauk and Fox, 2010; Kollmann et al., 2022), their associated synchrotron emission so far remains undetected. This is likely due to the weaker magnetic fields, which place their emission below the Earth's ionospheric cutoff (Equation 5; Hegedus et al., 2020; Marc et al., 2024), and/or lower particle energies. The prominent ring around Saturn is also thought to inhibit the build-up of energetic electrons in its radiation belt (Roussos et al., 2014). Finally, while Mercury in principle could also have a radiation belt (Lukashenko et al., 2020), its magnetosphere is very small due to its weak field and proximity to the Sun (Bagenal, 2013). The BepiColombo mission may soon shed new light on this topic (e.g. Williamson et al., 2026).

## 3 Radio emission from exoplanets and ultracool dwarfs

The prevalence of auroral radio emission from the magnetised Solar System planets naturally suggests that exoplanets could also be radio emitters. Additionally, GHz radio emission reminiscent

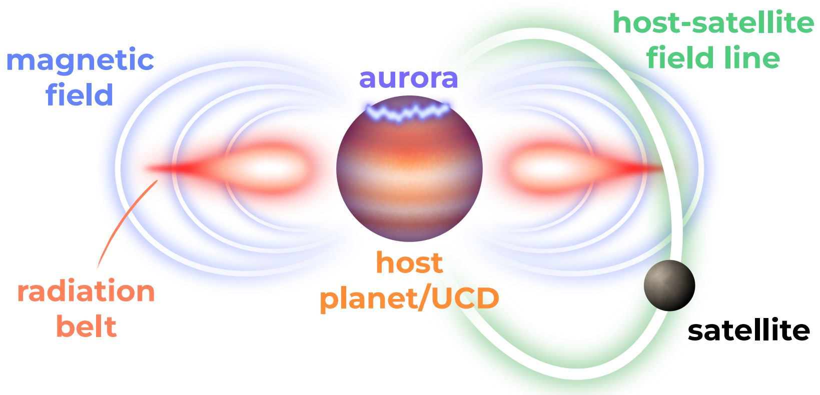


**Figure 1:** Sketch highlighting the different windows for studying and characterising exoplanets and ultracool dwarfs (UCDs) with the SKA. In the center, we see a magnetised planet/UCD. Electrons accelerated within the magnetic field lines can produce bright 'auroral' radio emission near the magnetic poles. This auroral emission can facilitate the detection and characterisation of magnetised exoplanets and UCDs. Strong magnetic fields can also trap relativistic electrons in a surrounding radiation belt that produces synchrotron radio emission, offering an additional detection pathway for UCDs. There are a variety of potential sources of the energetic electrons powering the radio emission, such as plasma outflow from a nearby star. Another source could be an orbiting satellite that is outgassing material, which forms an equatorial disk that the host's magnetic field interacts with. Satellites orbiting these objects can also induce astrometric motion in the radio emission of the host, which could be spatially-resolved using very long baseline interferometry. This presents the opportunity to detect unseen satellites. The same technique can also be applied to a radio-emitting host star.

of that seen on the magnetised Solar System planets has been detected from UCDs for over two decades. In this Section, we give an overview of the expected radio signatures from exoplanets, as well as those observed from UCDs. A graphical overview of the radio emission expected from exoplanets and UCDs is also provided in Figure 1.

### 3.1 Exoplanets

Many of the exoplanets discovered to date are giant planets[2] in short orbits around Sun-like stars – main-sequence stars with masses between 0.075 and $\sim$ 1.8 solar masses (Robrade and Schmitt, 2009; Chabrier et al., 2023). Like our Sun, these stars possess magnetically-heated coronae that drive outflows of material called stellar winds (Shoda et al., 2023). Giant close-in planets intercept much higher stellar wind fluxes than the Solar System planets. If the established radio-magnetic scaling law holds for these systems, these planets could exhibit bright radio aurorae (Zarka et al., 1997; Zarka, 1998, 2025).

The expectation of bright radio aurorae from giant, short-orbit planets has spurred a number of radio campaigns aimed at detecting these signatures (e.g. Lazio and Farrell, 2007; Smith et al., 2009; Lazio et al., 2010; Hallinan et al., 2013; Murphy et al., 2015; Lynch et al., 2018). Despite these efforts, a conclusive detection remains at large (although see Turner et al., 2021; Zhang et al.,

[2] Planets with masses greater than $\sim$ 10 Earth masses – the estimated upper limit for a planet with a rocky composition (Parc et al., 2024).

2025, for tentative results). A number of reasons have been proposed to explain this (Callingham et al., 2024). For instance, the stellar wind conditions of Sun-like stars are notoriously difficult to constrain (Wood et al., 2021), inhibiting accurate predictions for their expected radio powers via Equation 3. Dense stellar winds and extended planetary atmospheres could also attenuate or even inhibit the generation of auroral emission (Vidotto and Donati, 2017; Daley-Yates and Stevens, 2018; Weber et al., 2018; Kavanagh et al., 2019). The transient nature of auroral emission (Hess and Zarka, 2011; Lamy et al., 2023) also implies that unfavourable geometry and/or insufficient phase coverage could hinder detection of radio emission from exoplanetary systems, although this is becoming less of an issue with the advent of long-term wide-field radio monitoring (e.g. Callingham et al., 2021; Tasse et al., 2026). Radio frequency interference also poses a significant challenge in searching for exoplanet aurorae comparable to that of Jupiter (Cordun et al., 2025).

One of the major reasons inhibiting a conclusive detection of an exoplanet's aurora is arguably the ambiguity about their magnetic field strengths. Magnetic fields are thought to be prevalent on giant exoplanets (Brain et al., 2024), as they have sufficiently large reservoirs of conductive fluid that can convect and generate the field via dynamo action. While it is thought that the magnetic field strength of any planet scales with its internal heat flux provided it rotates sufficiently fast (Christensen et al., 2009), estimates for giant planets range from around 0.1 G to 1 kG depending on their age, stellar irradiation, and conductivity (Reiners and Christensen, 2010; Yadav and Thorngren, 2017; Zaghoo and Collins, 2018; Kilmetis et al., 2024). These quantities are generally poorly constrained or unknown for exoplanets. Additionally, the validity of these estimates have been disputed more recently (Kao et al., 2016; Kavanagh et al., 2024). These uncertainties mean that the appropriate observing frequency for detecting a given exoplanet's aurora is largely unconstrained (Equation 1).

The existence of magnetic fields on rocky planets is more uncertain, as the conditions to sustain a dynamo strongly depend on the planet's interior structure and composition (e.g. Blaske and O'Rourke, 2021). Even if the conditions are suitable, Bonati et al. (2021) estimated that the magnetic fields of rocky planets are at most 10 times as strong as that of the Earth (around 3 G), placing their auroral emission below 8 MHz. Since the high density of free electrons in the Earth's ionosphere reflects radio waves with frequencies below 10 MHz, detecting aurorae on rocky exoplanets will likely require space-based radio infrastructure (e.g. Burns et al., 2021; Knapp et al., 2024).

We note that auroral emission from the known exoplanet population could also be driven by co-rotation breakdown or sub-Alfvénic interactions with a satellite. However, both of these mechanisms require the presence of a satellite such as an exomoon, which so far have yet to be detected (Heller and Hippke, 2024; Kipping et al., 2025). Additionally, these mechanisms are not thought to produce observable fluxes without assuming extreme conditions (e.g. Nichols, 2011). Therefore, we do not consider these scenarios any further. Planets orbiting close to their host stars are also thought to generate aurora-like emission on the star via sub-Alfvénic interactions (Saur et al., 2013). However, this topic is covered in detail in Vedantham et al. (2026).

Finally, radiation belt emission is also possible for exoplanets. However, Jupiter's belt emission is over 5 orders of magnitude weaker than its auroral emission. As we will show in Section 4.2, the number of exoplanets with aurorae that are expected to be within the detection capabilities of the

SKA is low. Therefore, if these planets have Jupiter-like radiation belts, they are likely going to be very challenging to detect even for the SKA.

### 3.2 Ultracool dwarfs

Unlike exoplanets, radio emission has been detected from UCDs for over two decades (Berger et al., 2001). They generally show two distinct forms of emission: bright, short-duration, circularly-polarised bursts, and weakly polarised quiescent emission. The consensus is that the bursting emission is driven by auroral processes, whereas the quiescent emission is thought to be synchrotron emission originating from radiation belts (Kao et al., 2023; Climent et al., 2023). In the absence of conclusive radio detections from exoplanets, UCDs serve as suitable analogues to study magnetic field generation at planetary scales.

So far, the bulk of radio detections of UCDs have come at GHz frequencies (Williams, 2018), although advances at low radio frequencies have begun to discover emission from UCDs in the MHz regime (Zic et al., 2019; Vedantham et al., 2020, 2023; Yiu et al., 2025). Their GHz auroral emission implies that UCDs have magnetic fields that are up to a few kilogauss in strength, orders of magnitude stronger than that of Jupiter (Equation 1). This is thought to be due to their large internal heat fluxes which drive convection and generate their magnetic fields via dynamo action (Christensen et al., 2009; Reiners and Christensen, 2010). While UCDs are generally expected to harbour dipolar magnetic fields (Christensen et al., 2009), complex field topologies have also been inferred in some cases (e.g Lynch et al., 2015; Kao et al., 2016).

Estimates from volume-limited surveys indicate that $\sim$ 5% of all UCDs exhibit auroral radio emission detectable with current radio telescopes (Route and Wolszczan, 2016b). Their auroral bursts typically repeat over timescales consistent with their rotation periods inferred from their photometric variability (Pineda et al., 2017). This is reminiscent of Jupiter's auroral radio emission that is controlled by its interactions with the solar wind, its rotation, and its surrounding plasma disk (Marques et al., 2017; Zarka et al., 2021). Unlike Jupiter however, auroral UCDs are not found orbiting Sun-like stars, implying that their emission is powered by plasma disk interactions (Hallinan et al., 2015). The strong dependence of UCD radio aurorae on rotation is also apparent from the onset of their radio detectability at rotation periods less than $\sim$ 3 hours (Pineda et al., 2017). Theoretical models also predict that the brightness of aurorae arising from plasma disk interactions increases with the square of the object's rotation rate (Nichols, 2011; Saur et al., 2021).

The powerful magnetic fields of UCDs also make them effective traps for energetic particles that can form radiation belts. Very recently, Kao et al. (2023) and Climent et al. (2023) spatially-resolved the quiescent emission of the UCD LSR J1835+3259, unveiling a bipolar structure that bears a striking resemblance to Jupiter's radiation belt (Bolton et al., 2002). This object's auroral emission however remains unresolved, consistent with a compact source size. These results have cemented the paradigm for the Jupiter-like nature of radio emission from UCDs. Follow-up studies aimed at detecting the linearly-polarised component of radiation belt emission from UCDs will help to further solidify this hypothesis.

Despite the prevalence of radio emission from UCDs, the plasma source necessary to drive their emission is a mystery. The Jupiter-like nature of their emission naturally suggests that radio-emitting

UCDs are orbited by outgassing satellites. This is supported by planet formation theory, which predicts that UCDs are orbited by rocky planets (Liu et al., 2020). Additionally, rocky close-in planets orbiting UCDs are expected to undergo outgassing due to tidal forces (Barr et al., 2018) and/or induction heating in the presence of the strong magnetic fields of UCDs (Kislyakova et al., 2023). If satellites do orbit radio-emitting UCDs, the auroral signature is expected to also be modulated at the satellite's orbital period, as is seen for the Io-induced radio aurora on Jupiter (Marques et al., 2017; Kavanagh and Vedantham, 2023). However, radio aurorae on UCDs so far have only been found to be rotationally modulated. This does not rule out a satellite-driven origin explicitly. For instance, the plasma disk interaction could outshine the satellite-induced signal. Alternatively, certain geometric configurations can produce satellite-induced signals that are modulated at the rotation rate of the UCD and not the satellite's period (see Figure 2).

Other scenarios have also been inferred to explain the radio signatures from UCDs. At younger ages and higher masses, it becomes difficult to determine whether a UCD is a brown dwarf or a star. In the latter case, the UCD may still exhibit coronal activity (Paudel et al., 2020; Magaudda et al., 2024), which could result in stochastic flaring or even a quiescent stellar wind outflow. Both scenarios could load the UCD's magnetosphere with the plasma necessitated by their radio emission (Leto et al., 2021). However, this picture is difficult to reconcile for objects with spectral types later than mid L. Alternatively, lightning in the atmospheres of UCDs may liberate electrons that are supplied to the magnetosphere (Helling et al., 2011), although whether such events could supply the number of electrons necessary to sustain the observed radio emission from UCDs is unclear.

In Table 1, we list the relevant properties of each individual UCD with detected radio emission. Objects in binaries/multiple systems are only listed if their radio emission has been associated with a specific component. There are numerous examples of radio detections from systems containing UCDs where the emitting component has not been identified (Kao and Pineda, 2025). However, it is not clear in these cases which component emits or if multiple components contribute by different amounts. Therefore, we choose to exclude them for our purposes. The frequency and flux densities listed are indicative values, and can vary in time and frequency.

## 4 Detecting exoplanet aurorae with the SKA

As discussed in Section 3.1, radio emission from exoplanets that is detectable with the SKA is likely limited to auroral emission from magnetised giant planets, with the most plausible driver of their emission being arguably the winds of their host stars. The state-of-the-art for predicting the strength and frequency of this emission involves solving the magnetohydrodynamics equations describing the stellar wind outflow in three dimensions (e.g. Vidotto et al., 2012; Kavanagh et al., 2019; Elekes and Saur, 2023). However, these models are computationally expensive, and the information required to construct them (such as the surface magnetic field topology of the host star) is generally only available in a handful of cases. Lacking this information, simpler stellar models such as the isothermal model developed by Parker (1958) can provide sufficiently accurate results. This model assumes that the plasma temperature is constant from the stellar corona outwards. The benefit of the isothermal model is that it only depends on two parameters, and can be computed rapidly for a large set of parameters. In this Section, we use this model to predict the emission

**Table 1:** The catalogue of individual radio-detected UCDs listed in order of discovery. The columns list each UCD's name, spectral type (SpT), distance ($d$), rotation period inferred from its photometric variability ($P_{\rm rot}^{\rm phot}$) and radio bursts ($P_{\rm rot}^{\rm radio}$) rounded to two decimal places (if available), detected quiescent flux density ($F_{\rm Q}$) and frequency ($\nu_{\rm Q}$), and burst flux density ($F_{\rm B}$) and frequency ($\nu_{\rm B}$). The last column lists the reference for the discovery paper, followed by the references for SpT, $d$, $P_{\rm rot}^{\rm phot}$, $P_{\rm rot}^{\rm radio}$, $F_{\rm Q}$ & $\nu_{\rm Q}$, and $F_{\rm B}$ & $\nu_{\rm B}$. The values in brackets following the rotation periods are the errors on the least significant digit(s). Of the 24 objects listed, 21 exhibit quiescent emission, and 17 exhibit burst emission. Names superscripted with a † have been shortened, with the full names listed at the end of the Table. Entries denoted with "–" have no reported values.

| Name | SpT | $d$ (pc) | $P_{\rm rot}^{\rm phot}$ (hr) | $P_{\rm rot}^{\rm radio}$ (hr) | $F_{\rm Q}$ (µJy) | $\nu_{\rm Q}$ (GHz) | $F_{\rm B}$ (µJy) | $\nu_{\rm B}$ (GHz) | References |
|---|---|---|---|---|---|---|---|---|---|
| LP 944-20 | M9 | 6.427 | 3.84 | – | 100 | 8.5 | 2600 | 8.5 | 1, 2, 3, 4, –, 1, 1 |
| TVLM 513† | M8.5 | 10.734 | 1.96 | 1.96 | 464 | 8.44 | 5000 | 8.44 | 5, 2, 3, 4, 6, 6, 6 |
| J0036+18† | L3.5 | 8.736 | 2.7(3) | 3.08(5) | 240 | 8.46 | 500 | 4.88 | 5, 2, 3, 7, 8, 5, 8 |
| BRI 0021† | M9.5 | 12.446 | 3.05 | – | 25 | 8.46 | 360 | 8.46 | 5, 2, 3, 9, –, 5, 5 |
| J1048-39† | M8 | 4.045 | – | – | 140 | 4.8 | 29600 | 8.64 | 10, 2, 3, –, –, 10, 10 |
| LHS 3003 | M7 | 7.053 | – | – | 270 | 4.8 | – | – | 10, 2, 3, –, –, 10, – |
| J1835+32† | M8.5 | 5.689 | 2.84 | 2.84(1) | 722 | 8.44 | 2500 | 8.44 | 11, 2, 3, 4, 8, 8, 8 |
| J0523-14† | L2.5 | 12.734 | – | – | 231 | 8.46 | – | – | 11, 2, 3, –, –, 11, – |
| LP 349-25 A | M8 | 14.128 | – | – | 200 | 5 | – | – | 12, 13, 3, –, –, 13, – |
| LP 349-25 B | M9 | 14.128 | – | – | 110 | 5 | – | – | 12, 13, 3, –, –, 13, – |
| J0746+20 A† | L0 | 12.352 | 3.32(15) | 3.2(2) | 71 | 5 | 500 | 5 | 14, 15, 15, 16, 15, 15, 15 |
| J0746+20 B† | L1.5 | 12.352 | 2.07 | 2.1(1) | 138 | 5 | 1000 | 5 | 14, 15, 15, 17, 15, 15, 15 |
| J1314+13 B†,a | M7 | 16.39 | – | – | 1000 | 5 | 7000 | 5 | 18, 2, 19, –, –, 19, 19 |
| J1047+21† | T6.5 | 10.56 | 1.74(1) | 1.76(1) | 9 | 6 | 1550 | 5 | 20, 2, 21, 22, 23, 23, 23 |
| J1906+40† | L1 | 16.759 | 8.9 | – | 16.5 | 5 | – | – | 24, 2, 3, 24, –, 24, – |
| J0136+09† | T2.5 | 6.118 | 2.39 | $2.88^{+0.34}_{-0.27}$ | 11.2 | 10 | 51.5 | 10 | 21, 2, 3, 26, 27, 27, 27 |
| J1043+22† | L8 | 16.4 | – | $2.21^{+0.14}_{-0.13}$ | 16.3 | 6 | 69.0 | 6 | 21, 2, 21, –, 27, 21, 21 |
| J1237+65† | T6.5 | 10.42 | – | $2.28^{+0.10}_{-0.09}$ | 27.8 | 10 | 160 | 10 | 21, 2, 21, –, 27, 27, 27 |
| J0607+24† | L8 | 7.243 | – | – | 15.6 | 6.05 | – | – | 25, 2, 3, –, –, 25, – |
| J1122+25† | T6 | 17.7 | – | 1.93 | – | – | 2000 | 5 | 28, 2, 29, –, 29, –, 28 |
| J1750-00† | L4.5 | 9.210 | – | – | 56.4 | 6 | 667 | 6 | 30, 30, 3, –, –, 30, 30 |
| Elegast†,b | T6.5 | 65 | – | – | 1100 | 0.144 | – | – | 31, 31, 31, –, –, 31, 31 |
| J0623-04† | T8 | 11.44 | – | 1.91(1) | – | – | 3000 | 2.1 | 32, 32, 32, –, 32, –, 33 |
| J0752+16† | M7 | 18.881 | 21.21(5) | – | – | – | 130 | 9 | 34, 34, 3, 34, –, –, 34 |

*References* – 1: Berger et al. (2001), 2: Pineda et al. (2017), 3: Gaia Collaboration et al. (2023), 4: Miles-Páez et al. (2023), 5: Berger (2002), 6: Hallinan et al. (2007), 7: Metchev et al. (2015), 8: Hallinan et al. (2008), 9: Dulaimi et al. (2023), 10: Burgasser and Putman (2005), 11: Berger (2006), 12: Phan-Bao et al. (2007), 13: Curiel et al. (2024), 14: Antonova et al. (2008), 15: Zhang et al. (2020), 16: Harding et al. (2013), 17: Berger et al. (2009), 18: McLean et al. (2011), 19: Williams et al. (2015a), 20: Route and Wolszczan (2012), 21: Kao et al. (2016), 22: Allers et al. (2020), 23: Williams and Berger (2015), 24: Gizis et al. (2013), 25: Gizis et al. (2016), 26: Artigau et al. (2009), 27: Kao et al. (2018), 28: Route and Wolszczan (2016a), 29: Williams et al. (2017), 30: Richey-Yowell et al. (2020), 31: Vedantham et al. (2020), 32: Rose et al. (2023), 33: Kavanagh et al. (2024), 34: Magaudda et al. (2024)

† *Full names* – TVLM 513-46546, LSPM J0036+1821, BRI 0021-0214, DENIS J104814.6-395606, LSR J1835+3259, 2MASS J05233822-1403022, 2MASS J07464256+2000321 A, 2MASS J07464256+2000321 B, 2MASS J13142039+1320011 B, 2MASS J10475385+2124234, WISEP J190648.47+401106.8, SIMP J013656.5+093347.3, 2MASSI J1043075+222523, 2MASS J12373919+6526148, WISEP J060738.65+242953.4, WISEP J112254.73+255021.5, 2MASS J17502484-0016151, BDR J1750+3809, WISE J062309.94-045624.6, 2MASS J07522390+1612157

*Other notes* – *a*: The quiescent and bursting values quoted for J1314+13 B come from Williams et al. (2015a), who do not spatially-resolve the binary. However, Forbrich et al. (2016) later showed that component B is the only detectable radio emitter in the system, so we assume the emission reported by Williams et al. (2015a) also originated from component B. *b*: While this UCD does not show bursting emission, its quiescent emission is fully circularly polarised, a characteristic generally associated with auroral emission processes (see Vedantham et al., 2020).

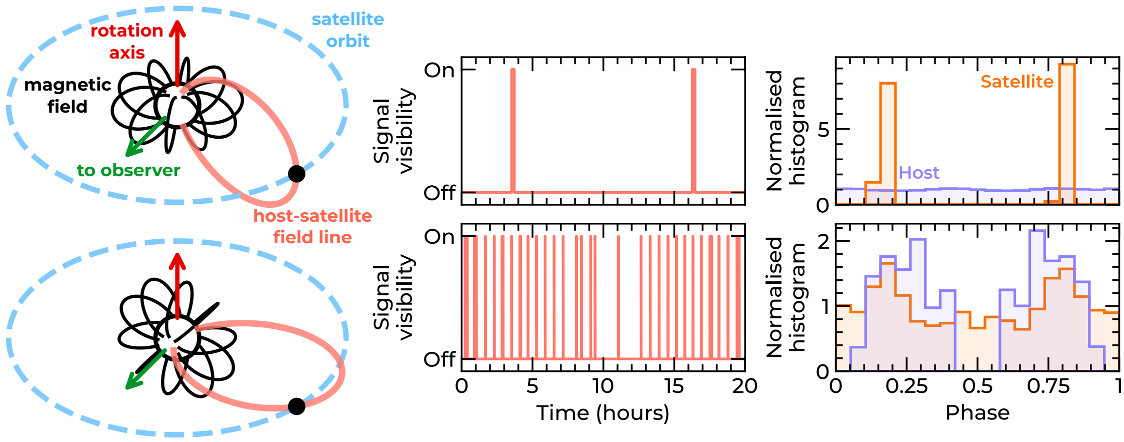


**Figure 2:** The periodicity of satellite-induced radio emission on a magnetised host for different geometric configurations. The top panels correspond to the configuration where the rotation and magnetic axes of the host (in this case, a UCD) are aligned, whereas the bottom panels show the case where they are misaligned by 90 degrees. The left panels show to-scale sketches of each configuration, and the middle panels show the visibility of the satellite-induced signal over time for each configuration, computed using the `MASER` code (Kavanagh and Vedantham, 2023). The right panels show the normalised histograms of the phases of the satellite's orbit and the rotation of the UCD when the signal is visible. In the aligned configuration, the signal is predominantly modulated with the satellite's orbital period, whereas in the misaligned configuration, the signal is predominantly modulated at the UCD's rotation period. A misaligned configuration could explain the phenomenon of radio aurorae on UCDs being modulated at the UCD's rotation period. The same phenomenon is also applicable to magnetically-interacting stars and planets (see Vedantham et al., 2026). The UCD is 10 Jupiter masses, 1 Jupiter radius, has a rotation rate of 1.28 hours and a dipole field strength of 1 kG, and is seen edge-on. The satellite's orbit is aligned with the UCD's rotation axis, and has an orbital period of 20 hours. The observing frequency is 1 GHz, and the ECM emission cone has an opening angle of 75° and a thickness of 2°. The histograms are computed for an observing window of 1 000 hours with 100 000 points.

strength and frequency of all known giant exoplanets and assess their detectability with the SKA.

### 4.1 Stellar wind prescriptions for known exoplanet hosts

To predict the wind-driven auroral emission of each giant exoplanet, we take a similar approach to Grießmeier et al. (2007) and Mauduit et al. (2023). We first use the code developed by Kavanagh and Vidotto (2020) to obtain the stellar wind velocity profile for each system as described by Parker (1958). For a given stellar mass and coronal (wind) temperature ($T$), we obtain the wind velocity $u_\mathrm{w}$ as a function of distance from the star $r$. We then compute the mass density profile of the wind via the conservation of mass:

$$\rho_\mathrm{w} = \frac{\dot{M}}{4\pi r^2 u_\mathrm{w}}, \tag{6}$$

where $\dot{M}$ is the stellar wind mass-loss rate. With this, we compute the pressure exerted by the stellar wind on each exoplanet:

$$p_\mathrm{w} = \rho_\mathrm{w}(a^2 + \Delta u^2) + \frac{{B_\mathrm{w}}^2}{2\mu_0}. \tag{7}$$

Here $a$ is the sound speed, which depends on the temperature $T$:

$$a = \sqrt{\frac{2k_\mathrm{B}T}{m_\mathrm{p}}}, \tag{8}$$

where $k_\mathrm{B}$ is Boltzmann's constant and $m_\mathrm{p}$ is the proton mass.

For the magnetic field strength of the wind $B_\mathrm{w}$, we follow the same approach as described in Section 2.2 of Vedantham et al. (2026). Within the region where the wind's magnetic pressure dominates, i.e.

$$\frac{{B_\mathrm{w}}^2}{2\mu_0} > \rho_\mathrm{w}{u_\mathrm{w}}^2, \tag{9}$$

we describe the magnetic field as a closed dipole, whose axis is aligned with both the stellar rotation and planetary orbital axes:

$$B_\mathrm{w} = \frac{B_\star}{2}\left(\frac{R_\star}{r_\mathrm{orb}}\right)^3. \tag{10}$$

Here, $B_\star$ is the dipole field strength of the star at its magnetic poles, $R_\star$ is the stellar radius, and $r_\mathrm{orb}$ is the planet's orbital distance. In this configuration, $B_\mathrm{w}$ points in the meridional direction. Then outside the magnetically-dominated region, we assume the wind magnetic field is purely radial:

$$B_\mathrm{w} = \frac{B_\star}{2}\left(\frac{R_\star}{r_\mathrm{orb}}\right)^2. \tag{11}$$

With the wind velocity and magnetic field profiles obtained for each exoplanet, we then compute the power dissipated onto the planetary magnetosphere via Equations 3 and 4. The isothermal wind model used assumes that the wind flows radially outward, perpendicular to the planet's orbital direction. This gives $\Delta u = \sqrt{{u_\mathrm{w}}^2 + {u_\mathrm{p}}^2}$, where $u_\mathrm{p}$ is the planet's orbital velocity. If the planet is in the closed-field region, the angle $\theta$ between $\Delta u$ and $B_\mathrm{w}$ is 90°. In the open-field region on the other hand, $u_\mathrm{w}$ is parallel to $B_\mathrm{w}$, so $\theta$ is the angle between $u_\mathrm{w}$ and $\Delta u$. To determine if the wind magnetic field is open or closed at the planet's position for a given $B_\star$, we check if Equation 9 is true assuming a closed field configuration, since the open field strength drops off more slowly as a function of distance than the closed field. Note that we do not account for the rotation of the star here, which will induce an azimuthal component to both the wind velocity and magnetic field (e.g. Weber and Davis, 1967) and alter the angle $\theta$.

We assume that some fraction $\varepsilon$ of the magnetic power intercepted by each planet's magnetosphere is dissipated over a bandwidth $\Delta\nu$, producing radio emission that is beamed outwards with a solid angle $\Omega$ and received at a distance $d$ (Grießmeier et al., 2007):

$$F = \frac{\varepsilon P_\mathrm{mag}}{d^2\Omega\Delta\nu}. \tag{12}$$

If the emission bandwidth $\Delta\nu = \nu_\mathrm{max} - \nu_\mathrm{min}$ is sufficiently wide ($\nu_\mathrm{max} \gg \nu_\mathrm{min}$), then $\Delta\nu \approx \nu_\mathrm{max}$. The maximum emission frequency corresponds to the cyclotron frequency where a dipolar field line of size $R_\mathrm{m}$ meets the surface (Vidotto and Donati, 2017):

$$\Delta\nu \approx \nu_\mathrm{max} = 2.8\left(\frac{B_\mathrm{p}}{1\ \mathrm{Gauss}}\right)\left(1 - \frac{3R_\mathrm{p}}{4R_\mathrm{m}}\right)^{1/2}\ \mathrm{MHz}. \tag{13}$$

If $R_m$ is sufficiently large, $\Delta\nu \propto B_p$, giving the following scaling relation for the auroral radio flux density:

$$F \propto \left(\frac{R_p}{d}\right)^2 B_p{}^{-1/3} B_w{}^2 \Delta u^2 p_w{}^{-1/3}. \tag{14}$$

### 4.2 Expected detection yields for aurorae on giant exoplanets

We now compute the expected flux density and frequency of aurorae of all known giant exoplanets as described in Section 4.1. We obtain the value of each planet's orbital period ($P_{orb}$), radius ($R_p$), and (minimum) mass ($M_p$), as well as the stellar mass ($M_\star$) and radius ($R_\star$) and the distance ($d$) to the system from the Default Parameter Set of the NASA Exoplanet Archive[3]. We compute the planet's orbital distance using the orbital period and stellar mass via Kepler's third law, neglecting the planet's eccentricity.

We filter out systems where the values for $P_{orb}$, $M_\star$, $R_\star$ or $d$ are missing. If a planet's radius is not known, we compute it via their (minimum) mass (if available) as described in Parc et al. (2024). In the cases where the mass is a minimum mass, then the radii computed using it is also a lower limit. We then discard those which are not giant planets (those with masses below 10 Earth masses). We also limit our calculations to systems where the host star is Sun-like, as they are both the most common exoplanet hosts and have thermal winds as described by the model deployed from Parker (1958) (Section 3.1). We note however that evolved stars with dense stellar winds could power aurorae on exoplanets that are much brighter than those possible for main sequence stars (Fujii et al., 2016). To determine if the host star is 'Sun-like', we compare the physical properties of each star to those estimated from main sequence relations derived as functions of stellar mass. From 0.076 to 0.616 solar masses, we use the absolute visual magnitude relation given in Equation 10 of Benedict et al. (2016), and above 0.616 solar masses we use the stellar radius and effective temperature relations given in Equations 3 and 4 of Eker et al. (2024). We consider the star to be on the main sequence if it is within one standard deviation of these relations. We also only consider systems where the stellar effective temperature is less than 8 000 K. Above this temperature, main-sequence stars no longer possess magnetically-heated coronae (Robrade and Schmitt, 2009), which are necessary to drive hot magnetised stellar wind outflows akin to that of the Sun. Finally, we discard systems with declinations outside the observing capabilities of the SKA (> +30°). These filtering steps bring the number of exoplanets from 6 028 down to 613.

For each exoplanet, we have four unknowns: the magnetic field strength of the host star $B_\star$, the wind temperature $T$ and mass-loss rate $\dot{M}$, and the planet's field strength $B_p$. As these parameters are all largely unconstrained, we explore two scenarios each for both the star and the planet. For each planet, we consider both a strong ($B_p$ = 100 G) and weak ($B_p$ = 25 G) field, corresponding to emission frequencies in the observing range of SKA-Low (Equation 1). For each star on the other hand, we consider an 'active' and 'inactive' state. For the active state, we adopt a strong surface magnetic field of 100 G and a wind mass-loss rate of 1000 $\dot{M}_\odot$, where $\dot{M}_\odot = 1.26 \times 10^{12}$ g s$^{-1}$ is the solar wind mass-loss rate (Cohen, 2011). The stellar magnetic field strength adopted here is representative of the dipolar magnetic field of an active planet-hosting star (e.g. Klein et al., 2021), and the mass-loss rate is comparable to the highest values inferred for Sun-like stars to date (Jardine

[3] NASA Exoplanet Archive (accessed on 10 Oct 2025)

and Collier Cameron, 2019). For the wind temperature, we use the maximum physical coronal temperature that gives a supersonic outflow at the stellar surface, which is necessary to drive the outflow (Kavanagh and Vidotto, 2020):

$$T < \frac{GM_\star m_\mathrm{p}}{4k_\mathrm{B}R_\star}. \tag{15}$$

For the systems we consider, this maximum temperature ranges from ~ 4 to 8 million Kelvin. The high temperature and large mass-loss rate assumed for the active state result in a fast and dense wind for each star, as are inferred for active low-mass main-sequence stars (Kavanagh et al., 2021). For the inactive state, we adopt a stellar magnetic field of 1 G, a mass-loss rate of 0.1 $\dot{M}_\odot$, and a coronal temperature of 0.5 MK.

We now compute the flux density and peak frequency of the aurorae on each giant planet as described in Section 4.1 for each combination of an active/inactive host star and strong/weak planetary magnetic field. In Equation 12, we assume a magnetic energy conversion efficiency of $\varepsilon = 2 \times 10^{-3}$ and a solid angle of $\Omega = 1.6$ sr, which are the inferred values from Solar System observations (Zarka et al., 2004; Zarka, 2007). Given the existing uncertainties on the properties considered here, we do not propagate the errors in the values taken from the NASA Exoplanet Archive.

In Figure 3, we show the expected flux density and peak frequency of the auroral emission on each giant exoplanet for a strong and weak planetary field. We only show the results assuming an active host star, as all systems for an inactive state are below the detection threshold of SKA-Low in configuration AA4 for an 8-hour image observation. While weaker planetary magnetic fields produce slightly higher fluxes (see Equation 14), the sensitivity of SKA-Low is significantly lower at the corresponding peak frequencies (~ 60 MHz). Additionally, conditions are more favourable for generating ECM emission if the field strength is higher (Section 2.1). We also note that absorption of the auroral emission by the wind of the host star is likely to be more severe at lower frequencies (Vidotto and Donati, 2017; Kavanagh et al., 2019). However, emission from planets around active stars may be absorbed substantially more than those around inactive stars, as active stars likely possess dense stellar winds (e.g. Jardine and Collier Cameron, 2019).

We also estimate the number of systems detectable with SKA-Low for different array configurations and observing times. For this, we compute the image noise of the SKA as outlined in Section 8 of Braun et al. (2019), linearly interpolating the array sensitivities for each frequency[4]. We consider a system to be detected if it reaches a signal to noise ratio (SNR) of 5 or greater. In Table 2 we list the number of systems detectable with SKA-Low in array configurations AA* and AA4, for observing times of 1 and 8 hours. Overall, prospects are more favourable in the strong field scenario and longer integration times. With weak planetary magnetic fields, the only planet detectable is $\tau$ Boo b, requiring at least an 8 hour integration for a conclusive detection. With strong planetary magnetic fields however (corresponding to higher frequencies, and consequently greater sensitivity), more planets become detectable. This implies that SKA-Mid could be better suited for detecting

[4] The most recent estimates for the sensitivities of SKA-Low and Mid are given in Tables 5 and 6 of the Anticipated SKA1 Science Performance document (Revision 002).

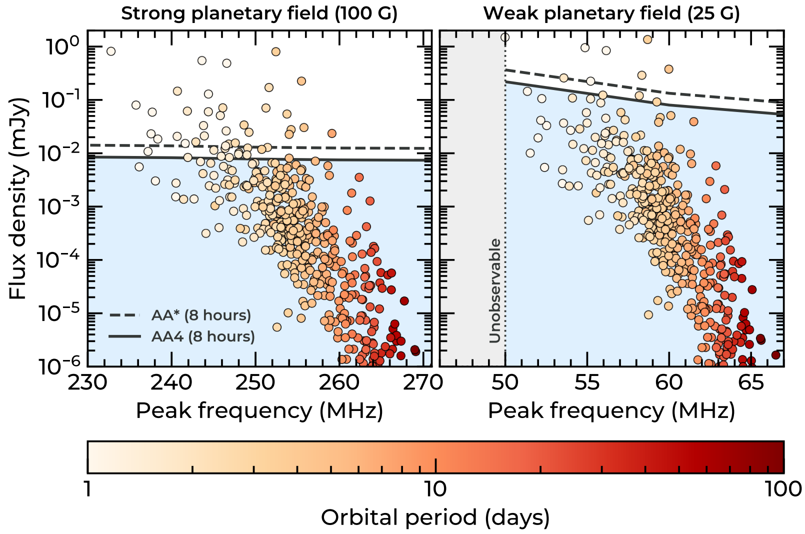


**Figure 3:** Predicted auroral radio signatures of the known giant planet population assuming their host stars are active, for a planetary magnetic field strength of 100 G (left) and 25 G (right). Each planet is coloured based on its orbital period. The detection thresholds of SKA-Low in the AA* and AA4 configurations for an 8-hour image exposure are also shown as dashed and solid lines.

exoplanets, although the field strengths detectable with SKA-Mid may only be attainable for young, massive Jupiter-like planets in wide (> 1 au) orbits (Kilmetis et al., 2024). Irrespective of the observing time and array configuration, the five brightest planets in the strong field regime are $\tau$ Boo b, TOI-2109 b, HIP 65 A b, WASP-18 b, and 51 Peg b. We note that the auroral signatures modelled here are likely short in duration due to the intrinsic beaming of the emission mechanism (Ashtari et al., 2022), which we do not account for. As a result, a single integration may smear out the signal. Therefore, conclusive detection may require stacking multiple observations of a given system.

While the prospects presented here for detecting exoplanet aurorae with the SKA are uncertain, wide field surveys at low frequencies will allow us to assess the uncertainties on the stellar wind, planetary magnetic field, conversion efficiency, and beaming geometry of each known exoplanet system at an unprecedented level. These surveys may also lead to the detection of aurorae from undetected planets, such as those with long periods in face-on orbits. Due to the uncertainties on the relevant physical parameters and beamed nature of the emission, blind surveys may be the most promising pathway to discovering exoplanet aurorae (e.g. Callingham et al., 2021; Tasse et al., 2026).

## 5 Detecting ultracool dwarf aurorae with the SKA

The observed radio aurorae on UCDs (Table 1) can inform us about their expected detection yields with the SKA, without utilising scaling laws that contain unknown parameters as in Section 4. With sufficient telescope sensitivity, the detectability of auroral emission is limited by the viewing and magnetic geometry (Hess et al., 2008; Louis et al., 2019; Kavanagh and Vedantham, 2023; Lamy

**Table 2:** The number of known giant exoplanets detectable with the SKA at an SNR > 5. Results are shown for the AA* and AA4 configurations of the SKA for different observing times and planetary field strengths. Note that these numbers are computed under the assumption that the host star of each planet is in an 'active' state, with a strong surface magnetic field and dense, fast stellar wind (see text).

| Planet field strength | 1 hour (AA*) | 8 hours (AA*) | 1 hour (AA4) | 8 hours (AA4) |
|---|---|---|---|---|
| Weak (25 G) | 0 | 1 | 0 | 3 |
| Strong (100 G) | 5 | 11 | 8 | 16 |

et al., 2023). On UCDs, auroral emission is generally interpreted as originating from either a shell of field lines (Leto et al., 2016; Pineda et al., 2017; Bloot et al., 2024; Guirado et al., 2025) or individual 'active field lines' (AFLs) within a dipolar (Kuznetsov et al., 2012; Bastian et al., 2022; Kavanagh et al., 2024) or multipolar field geometry (Lynch et al., 2015). Of all these different scenarios, the shortest visibility window for the emission is that on a single AFL. A number of numerical tools have been developed to compute the visibility of auroral emission from magnetised bodies like UCDs, such as `ExPRES` (Hess et al., 2008; Louis et al., 2019) and `MASER` (Kavanagh and Vedantham, 2023). The `CHARM`[5] framework recently developed by Kavanagh et al. (2024) contains different physical models for the origins of auroral emission within dipolar magnetic fields. `CHARM` is designed to efficiently explore large parameter spaces, making it well-suited for parametric inversion studies and Monte Carlo simulations. One such model included predicts emission from AFLs. In this Section, we use this model to estimate the detectability of the population of UCDs with the SKA, assuming they all exhibit radio aurorae.

### 5.1 Simulating a population of auroral UCDs

To estimate the number of UCD aurorae detectable with the SKA, we use the AFL model from `CHARM` to simulate the radio lightcurves of a population of UCDs within 300 pc, comparable to the scale height of the Milky Way (Aganze et al., 2022). There are a number of parameters required to use this tool. We describe our sampling method for each one below:

- *Viewing angle*: The viewing angle or inclination of the system is defined by the angle $i$ formed between our line of sight and the UCD's rotation axis. To randomly orient the rotation axis of each UCD, we uniformly sample $\cos i$ (Kavanagh and Vedantham, 2023).
- *Magnetic obliquity*: This describes the angle $\beta$ between the rotation and dipole axis of the UCD. While there may be an underlying distribution of magnetic obliquities relating to the dynamo processes on these objects, it is unknown. Therefore, we opt to uniformly sample $\beta$ from 0 to 90°.
- *Field strength*: Like the obliquity, there is presumably some underlying distribution of field strengths for UCDs, which is unknown. So far, UCD aurorae have been predominantly detected from $\sim 1$ to 20 GHz (Kao et al., 2018; Rose et al., 2023), corresponding to dipolar field strengths ($B_0$) of $\sim 350$ G to a few kG. To keep our estimates consistent with this range, we draw samples for $B_0$ from a log uniform prior ranging from 350 G to 10 kG. We note however that Vedantham et al. (2023) recently reported detection of auroral bursts from a binary UCD system at 144 MHz,

[5] `https://github.com/robkavanagh/charm`

suggesting that some UCDs may have magnetic fields much weaker than our adopted range.

- *Rotation period*: The rotation periods of UCDs with spectral types from mid-L to late-T are estimated to follow a log-normal distribution (Radigan, 2014):

$$f(P_{\rm rot}) = \frac{1}{P_{\rm rot}\sigma\sqrt{2\pi}} \exp\left\{-\frac{1}{2}\left(\frac{\ln P_{\rm rot} - \mu}{\sigma}\right)^2\right\}, \quad (16)$$

  where $P_{\rm rot}$ is in hours, $\sigma = 0.48$ and $\mu = 1.44$. While Route (2017) have extended this distribution to late-M UCDs, this can increase the risk of including UCDs that are above the hydrogen-burning limit. These UCDs likely possess coronae that drive stellar winds, which will spin down the UCD over time (e.g. Popinchalk et al., 2021). For instance, the most recently-detected radio-emitting UCD (the M7 J0752+16) has an estimated rotation period of 21 hours (Table 1). According to the distribution above, the probability of a UCD possessing a rotation period exceeding 20 hours is 0.05%. Additionally, an M7 UCD must be younger than $\sim$ 100 Myr in order to be below the hydrogen burning limit, whereas mid-Ls can have ages up to $\sim$ 1 Gyr (Davis et al., 2025). J0752+16 also does not show any lithium absorption (Wang et al., 2022), indicative of a stellar nature. Therefore, we draw the values of $P_{\rm rot}$ for each UCD from the distribution presented by Radigan (2014). We also note that a period of less than 1 hour is below the breakup limit for objects with masses less than 10 Jupiter masses.

- *Rotation phase*: At the start of each observation, we randomly choose the initial rotation phase of the UCD $\phi_0$ from 0 to $2\pi$. The rotation phase is then:

$$\phi_{\rm rot} = \phi_0 + \frac{2\pi t}{P_{\rm rot}} \quad (17)$$

  When $\beta \neq 0°$, the magnetic axis precesses about the rotation axis, with its position described by $\phi_{\rm rot}$ (Kavanagh et al., 2024).

- *Active field line properties*: The AFL is defined by its magnetic longitude $\phi_{\rm B}$ and spatial extent or 'loop size' $L_{\rm B}$ in the magnetic equator (Kavanagh et al., 2024). For the longitude, we uniformly draw values from 0 to $2\pi$, whereas for the loop size, we choose values from 1 to 100 times the radius. The physical meaning of the loop size relates to the region in the magnetosphere where the electrons are accelerated (e.g. Zarka et al., 2025). We currently do not have any means to place constraints on these values. This likely requires solving the magnetohydrodynamic equations describing the flow of plasma in the UCD's magnetosphere for different rotation rates and magnetic geometries.

- *Emission cone properties*: An ECM emission cone at a given frequency is defined by its opening angle $\alpha$ and thickness $\Delta\alpha$ (Louis et al., 2019). We opt for fixed values of $\alpha = 75°$ and $\Delta\alpha = 1°$, in line with those inferred for Jupiter (Hess et al., 2008; Lamy et al., 2021).

We also require the following parameters to estimate if the system is visible:

- *Distance*: We draw the distance to each UCD from 2 to 300 pc assuming a constant space density. We achieve this by drawing the volume $V$ of the spherical shell formed between 2 pc and $d$ from a uniform prior. The lower limit adopted for the distance is that of binary system Luhman 16, the closest known UCDs (Luhman, 2013).

- *Luminosity*: The radio luminosity $l$ of each UCD depends on its observed flux densities $F$ and distance $d$:
$$l = Fd^2, \tag{18}$$
which ranges from $\sim 2 \times 10^{11}$ to $2 \times 10^{14}$ erg s$^{-1}$ Hz$^{-1}$ for the UCDs listed in Table 1. For each simulated UCD, we sample $l$ from a log uniform distribution in this range, and then compute the received flux density by dividing by its sampled distance squared. This implicitly assumes that the solid angle of the emission is in the same range as for the detected UCDs, which should relate to the emission cone properties (see Equation 7 of Kavanagh et al., 2022).

- *Observing frequency*: We uniformly sample the observing frequency $\nu_{\rm obs}$ from 1 to 1.76 and 4.6 to 15.3 GHz, corresponding to the frequencies where UCD aurorae have been predominantly detected so far that are observable with the planned configuration of SKA-Mid. The observing frequency maps to the magnetic co-latitude of the emission cone along the AFL, which we compute as described in Kavanagh and Vedantham (2023).

With the required parameters established, we simulate the lightcurves of $10^6$ UCDs for observing times of 1 and 8 hours. We compute each lightcurve at a resolution of 1 second, and then re-bin to a resolution of 10 minutes. An example is shown in Figure 4. We then count the number of 10 minute bins that achieve an SNR > 5 as described in Section 4.2. We note that the AFL model produces both right and left circularly polarised signals (RCP and LCP). If the pulses overlap, they could result in a non-detection in Stokes V. However, for simplicity we assume that a detection is obtained provided either the RCP or LCP signal is bright enough, irrespective of whether they overlap. We also note that this effect can be circumvented if the observing bandwidth is sufficiently wide (Lamy et al., 2008b).

### 5.2 Expected detection yields of UCD aurorae

In Figure 5, we show the fraction of UCDs with aurorae detectable by SKA-Mid in configurations AA* and AA4 as a function of distance, for observing times of 1 and 8 hours. We estimate that 9.8 to 18.5% of all UCDs within 25 pc will be detectable with SNRs exceeding 5. The completeness is above 5% out to 60 to 120 pc, where the known population is very incomplete (Best et al., 2024), and drops below 1% at distances of around 150 to 250 pc. It is interesting to note that our estimated completeness within 25 pc is close to the 5-10% burst rate inferred from volume-limited surveys by Route and Wolszczan (2016b). This may indicate that most UCDs exhibit radio aurorae, but we only detect a fraction of them due to unfavourable geometry. To further explore this, we re-ran our simulation for $10^5$ UCDs within 25 pc, using a similar observing setup as Route and Wolszczan (2016b) (0.4 mJy noise, 5 GHz observing frequency, SNR detection threshold of 3). From this, we find that $3.3 \pm 0.5\%$ of the 25 pc sample are detectable. In other words, the occurrence rate of radio bursts on UCDs can be reproduced with our geometric prescription combined with the assumed priors on the magnetic and radio properties of UCDs.

In terms of the actual number of UCDs we expect to be detected with the SKA, the space density of UCDs within 25 pc with spectral types from M7 to M9.5 is estimated to be $7.1 \times 10^{-3}$ pc$^{-3}$ (Bardalez Gagliuffi et al., 2019), and $8.1 \times 10^{-3}$ pc$^{-3}$ from L0 to T8 (Best et al., 2024), giving a total space density of $15.2 \times 10^{-3}$ pc$^{-3}$. Given our computed completenesses out to 300 pc and the

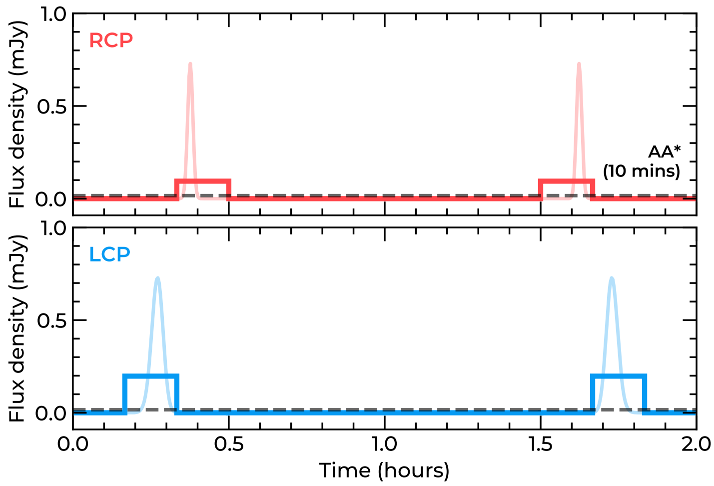


**Figure 4:** Example detection of auroral radio emission at 1 GHz from UCD at 12 pc with AA*. The top and bottom panels show the right and left circularly polarised signal respectively (RCP and LCP). The lighter thinner line in each panel show the auroral signal at a very high time resolution, and the darker stepped line shows the signal binned to a 10 minute resolution. The dashed horizontal line shows the sensitivity of AA* at 1 GHz for a 10 minute exposure computed as described in Section 4.2. At this resolution, the pulses reach SNRs of ~ 6 and 12 in RCP and LCP respectively. The parameters used are: $i = 90°$, $\beta = 10°$, $B_0 = 1$ kG, $P_{\rm rot} = 2$ hours, $\phi_{\rm rot,0} = 0$, $L_{\rm B} = 10$ radii, $\phi_{\rm B} = 0$, $\alpha = 75°$, $\Delta\alpha = 1°$, $l = 10^{13}$ erg s$^{-1}$ Hz$^{-1}$.

75% sky coverage of the SKA, we estimate that 1 600 to 8 000 will be detected, which is at least a two order of magnitude increase in the number of UCDs with detected aurorae.

Large radio transient surveys that will be carried out with the SKA will be key to delivering these estimated numbers. Source identification efforts will greatly benefit from the Euclid mission, which is anticipated to detect millions of UCDs within the thin disk of the Milky Way (Solano et al., 2021). The large statistics the SKA will deliver for radio-emitting UCDs will allow us to quantify the underlying demographics of their magnetic fields and radio emission. This will be particularly fruitful at lower frequencies with SKA-Low, which so far remains largely unexplored for UCDs (Zic et al., 2019; Vedantham et al., 2020, 2023; Yiu et al., 2025). Additionally, our estimated yields here assume a detection is achieved within an 8-hour window. Stacking observations covering multiple rotation phases of UCDs could allow for fainter targets to also be detected.

### 5.3 Demographics and detection biases for auroral UCDs

The large number of UCDs we anticipate the SKA will detect will allow us to explore underlying detection biases. For instance, Kavanagh et al. (2024) recently suggested that there should be a bias towards detecting radio aurorae on UCDs with certain viewing and magnetic geometries, analogous to the geometric bias expected for detecting magnetic star-planet interactions (Kavanagh and Vedantham, 2023). In Figure 6, we show the viewing angle against the magnetic obliquity of each UCD with a duty cycle exceeding 50% from the simulated 8 hour observations with AA4. We find a bi-modal distribution akin to that found by Kavanagh and Vedantham (2023). The two modes of this distribution describe two distinct geometric configurations for UCDs – an edge-on view with a low obliquity, and a pole-on view with a large obliquity. Both configurations enable

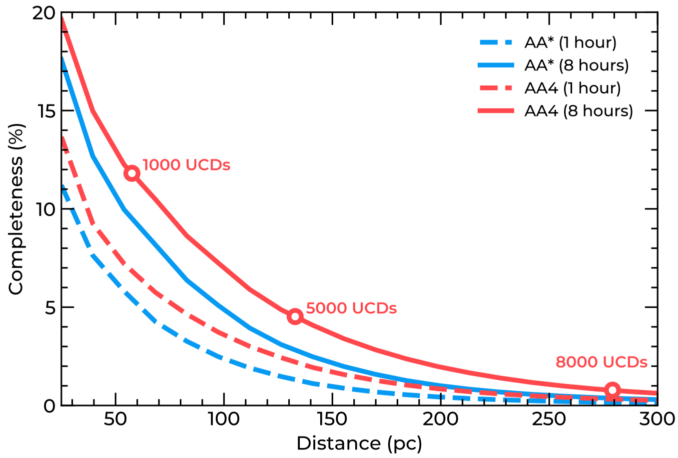


**Figure 5:** The estimated completeness of UCDs as a function of distance with aurorae detectable by SKA-Mid. Results are shown for both the AA* and AA4 configurations, for observing times of 1 and 8 hours. The distances where 1 000, 5 000, and 8 000 UCDs are detected are marked for the 8 hour observations with AA4, assuming the maximum 75% sky coverage of the SKA is achieved.

the magnetic axis to form the angle $\alpha$ with the line of sight over the UCD's rotation, providing favourable conditions for the emission cone to intersect the line of sight (Kavanagh and Vedantham, 2023; see also Section 2.3 of Vedantham et al., 2026).

UCD viewing angles can be inferred from their rotation periods and velocities (Vos et al., 2017), and their magnetic obliquities can be estimated via `CHARM` Kavanagh et al. (2024). Confirmation of the expected detection bias presented here will improve targeting strategies to boost detection yields. Comparison of the detected distribution of magnetic obliquities will also allow us to estimate the true underlying distribution, which will inform us about magnetic field generation on UCDs, and in turn their interior structures (Stanley and Bloxham, 2004).

In terms of the other parameters, we expect that nearby UCDs with strong magnetic fields, short rotation periods, and bright aurorae are more favourable for detection. Additionally, lower observing frequencies are favoured, as a wider range of magnetic field strengths can be seen. We caution however that the results presented here are dependent on a number of assumptions about the system priors and underlying magnetic geometry. The large statistics of UCDs delivered by the SKA will facilitate extracting the true distributions of radio and magnetic properties for UCDs.

## 6 Detecting ultracool dwarf radiation belts with the SKA

As for their auroral emission, we can use the observed levels of quiescent/radiation belt emission from UCDs to estimate their expected detection yields for the SKA. Additionally, the recent findings from Kao et al. (2023) and Climent et al. (2023) have unveiled the prospects for spatially-resolving the radiation belt emission of UCDs using very long baseline interferometry (VLBI). We explore these two scenarios for the SKA in Sections 6.1 and 6.2.

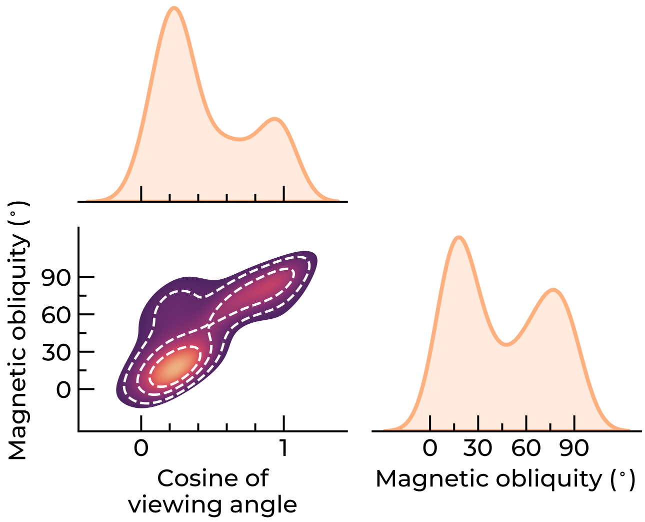


**Figure 6:** The geometric bias we expect for detecting auroral emission on UCDs with the SKA. The filled contour in the bottom left panel shows the bivariate kernal density estimation (KDE) above the 10th percentile for the magnetic obliquity and viewing angle of UCDs with duty cycles exceeding 50%. The dashed white lines show the 20th, 50th, and 80th percentiles. The two distinct geometric configurations of an edge-on view with a low obliquity and a pole-on view with a high obliquity can be clearly seen. The panels above and to the right show the univariate KDE of each variable. The data used here is that simulated for the 8 hour observations with AA4. Figure made using `seaborn.PairGrid` (Waskom, 2021).

### 6.1 Unresolved radiation belts

The observed unresolved quiescent radio luminosities of individual UCDs range from $\sim 4 \times 10^{10}$ to $4 \times 10^{14}$ erg s$^{-1}$ Hz$^{-1}$ (Table 1), and have been detected from 144 MHz to 100 GHz (Williams et al., 2015b; Vedantham et al., 2020). While synchrotron emission from a single electron is highly collimated (Rybicki and Lightman, 1986), radiation belt emission is comprised of synchrotron beams from many individual electrons with different phases, frequencies, and locations within the magnetosphere. As a result, the expected signature should not vary significantly as the UCD rotates, assuming the underlying population of relativistic electrons is stable. This means that detection of UCD radiation belt emission is more suited to single longer exposures, as opposed to the short cadence observations necessary to detect their aurorae.

To estimate the number of UCDs with unresolved radiation belts detectable by the SKA, we simulate emission from 1 million UCDs, uniformly sampling the log of the luminosity in the aforementioned range, the distance from 2 to 300 pc as described in Section 5.1, and the observing frequency from 144 MHz to 1.76 GHz and 4.6 to 15.3 GHz. We then compute the synthetic flux density observed via Equation 18, and count the number of systems with SNRs of 5 or greater as described in Section 4.2). We show the completeness as a function of distance in Figure 7. We estimate that 66 to 85% of UCDs within 25 pc are detectable with the SKA. This is significantly larger than the inferred rate of 15 to 20% for individual UCDs (Kao and Shkolnik, 2024). However, we assume that all UCDs possess radiation belt emission, which may not be the case. This contrasts with our

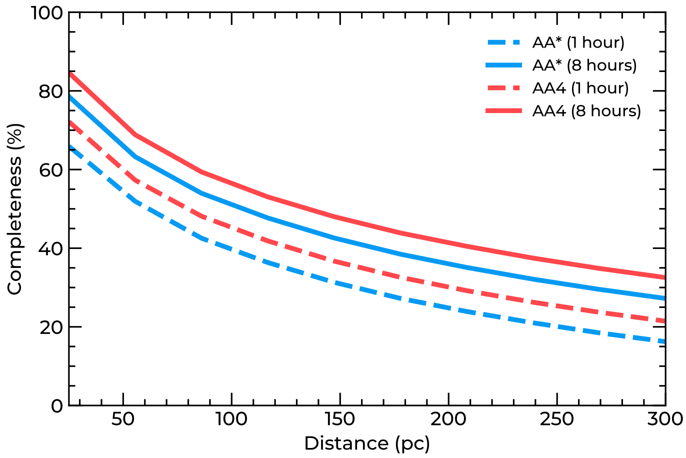


**Figure 7:** Same as Figure 5 but for unresolved radiation belt emission from UCDs.

findings in Section 5.2, which suggest that most UCDs possess auroral emission. Additionally, we assume that the lower limit on the luminosity is the lowest observed value, which skews our simulation towards bright UCDs only. Reducing the lower limit of the radio luminosity by three orders of magnitude, we obtain completeness rates of 40 to 50%. As for their auroral emission, the large number of UCDs with quiescent emission detected with the SKA will provide more robust estimates for these underlying distributions. We also note that Kao and Pineda (2025) recently showed that radiation belt emission is enhanced for UCDs in binaries. While the underlying cause of this enhancement remains unclear, this phenomenon can be exploited in the SKA era to achieve higher detection yields by targeting known binaries.

### 6.2 Resolvable belts around UCDs

SKA-Mid operating as a phased array within a global VLBI network will deliver sub-milliarcsecond (mas) resolution at GHz frequencies with an unprecedented sensitivity. This will provide the opportunity to spatially-resolve the radiation belt emission of nearby UCDs, a technique recently demonstrated for the UCD LSR J1835+3259 by Kao et al. (2023) and Climent et al. (2023). These images contain a wealth of information about UCDs, such as the large-scale magnetic field geometry and the energetic electron properties throughout their magnetospheres. Extracting this information will facilitate a better understanding of radiation belt emission detected from more distant UCDs, where spatially resolving the belt is no longer feasible. Temporal tracking of the radiation belt can also provide a direct measurement of the rotation periods of UCDs, which is generally only derivable if the UCD exhibits detectable photometric variability (Miles-Páez et al., 2023).

Forming a 10 000 km baseline with a 100-m dish, we expect that SKA-Mid will achieve a sensitivity at GHz frequencies of 4 μJy per beam for a 1 hour integration (Rioja and Dodson, 2020) and a spatial resolution of 1 mas. The spatial extent of the radiation belt around LSR J1835+3259 is $\sim$ 35 Jupiter radii (Climent et al., 2023), which we expect to be resolvable out to $\sim$ 17 pc. From our calculations in Section 6.1, we estimate that 78% of the UCDs within 17 pc have radiation belts with SNRs > 5. This corresponds to around 300 UCDs, assuming they all possess radiation belts.

## 7 Detection prospects via astrometric monitoring

So far, we have focussed on methods for directly detecting and characterising exoplanets and UCDs with the SKA. However, there are also viable pathways to indirectly study these objects. For instance, the SKA is ideally suited to detect magnetic interactions between exoplanets/UCDs with magnetised hosts (see Vedantham et al., 2026). Additionally, exoplanets and UCDs that orbit a radio-emitting star or UCD can induce astrometric motion in the radio centroid of the host which could be resolvable using the SKA in tandem with VLBI. This has already been demonstrated as a viable detection pathway for satellites using current radio telescopes (e.g. Forbrich et al., 2013; Curiel et al., 2020, 2022). Given the order of magnitude increase in sensitivity expected for sub-mas imaging with SKA-VLBI, long-term monitoring may unveil a wealth of previously undetected satellites to nearby radio-emitting UCDs and stars.

The angular shift or reflex motion induced by a satellite on a host is (Forbrich et al., 2013):

$$\theta = \frac{r_{\rm orb}}{d}\frac{M_{\rm sat}}{M_{\rm host}}, \tag{19}$$

where $r_{\rm orb}$ is the orbital distance, $d$ is the distance to the system, and $M_{\rm sat}$ and $M_{\rm host}$ are the masses of the satellite and host. At GHz frequencies, the $5\sigma$ astrometric accuracy of SKA-VLBI is estimated to be $\sim 0.5$ mas (Rioja and Dodson, 2020). In Figure 8, we show the parameter space of satellites corresponding to a reflex motion at this level. We show results for both a UCD host of 13 Jupiter masses (the lower limit for UCDs), and an M dwarf host of 0.2 solar masses, which are the most prevalent radio emitters on the main sequence (Driessen et al., 2024). In the UCD host case, a 10 Earth-mass planet in a 1000 day orbit is detectable within 22 pc. Prospects for detecting such planets are likely most favourable for UCDs with high duty cycles, such as those with persistent radiation belt emission. From our calculations in Section 6.1, we estimate that $\sim$ 680 UCDs are within 22 pc with radiation belts at a level detectable with SKA-VLBI (i.e. with fluxes above 40 µJy), again assuming they all possess radiation belts.

These results show the promise of SKA-VLBI for expanding the demographics of satellites around low-mass stars and UCDs. While formation theory predicts that UCDs likely host rocky planets (Liu et al., 2020), the intrinsic faintness of UCDs hinders their detectability with current technology. Astrometric detection of satellites is also biased towards face-on orbits (Smith et al., 2024; El-Badry et al., 2024), which cannot be detected via the transit or radial velocity methods. Radio monitoring of such systems may also unveil signatures of magnetic interactions between the host and satellite, which have favourable detection prospects in face-on systems (Kavanagh and Vedantham, 2023).

## 8 Looking towards operations

The uncertainties on the physical and geometric properties of exoplanets and ultracool dwarfs that underpin the brightness of their radio emission in frequency and time mean that their detection prospects for the SKA are most favourable for wide-field surveys with high time cadences. One approach could be to monitor specific regions of the sky via regular SKA Cycle proposals. Alternatively, wide field transient surveys akin to those being carried out with LOFAR will likely yield a large number of detections (Shimwell et al., 2022; Callingham et al., 2023). This however will be

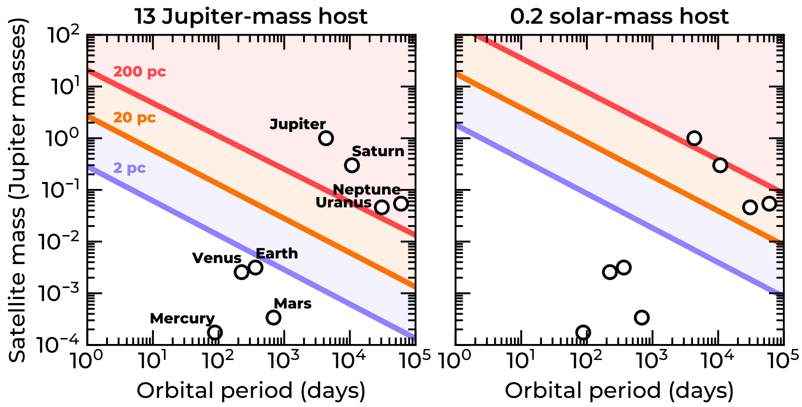


**Figure 8:** The parameter space of satellites around a radio-emitting host UCD (left) and an M dwarf star (right) that are detectable via astrometric monitoring with SKA-VLBI. The coloured lines show the detection limits at different distances, above which the satellite-induced astrometric motion exceeds 0.5 mas. The Solar System planets are overplotted for reference. Prospects for detecting exoplanets around radio-emitting UCDs are particularly favourable, with planets of a few Earth masses being detectable in orbits less than 1000 days for the closest systems.

a significant undertaking, and is likely at a level appropriate for a Key Science Project. Collaboration and efficient communication between different working groups will be key to maximising the science output for all in this case.

Targeted observations will also be a viable detection strategy in specific cases, such as for monitoring the most promising exoplanetary systems (e.g. Turner et al., 2021; Zhang et al., 2025) and the known population of radio-emitting UCDs. New candidate systems detected in surveys with the SKA and other operating radio telescopes may also be suited to targeted follow-up. Detecting satellites around nearby radio-emitting stars and UCDs through astrometry will also demand targeted monitoring over multiple years. Any one of these approaches will likely deliver unprecedented insights into the formation and evolution of extrasolar worlds.

## Acknowledgements

We thank the anonymous reviewer for their time and comments, which strengthened the cohesion of the chapter. RDK and JRC acknowledge funding from the European Union via the European Research Council (ERC) grant Epaphus (project number: 101166008). PZ and CKL acknowledge funding from the ERC under the European Union Horizon 2020 research and innovation programme (grant agreement no. 101020459 - Exoradio). RDK and HKV acknowledge funding from the Dutch Research Council (NWO) for the e-MAPS (Exploring Magnetism on the Planetary Scale) project (project number VI.Vidi.203.093) under the NWO talent scheme Vidi. HKV also acknowledges funding from the European Research Council under the European Union's Horizon Europe programme (grant number 101042416 STORMCHASER). AZ acknowledges support from ANID – Millennium Science Initiative Program – Center Code NCN2024_001 and Fondecyt Regular grant number 1250249.

## References

C. Aganze et al. *ApJ*, 934(1):73, July 2022. doi: 10.3847/1538-4357/ac7053.

K. N. Allers, J. M. Vos, B. A. Biller, and P. K. G. Williams. *Science*, 368(6487):169–172, Apr. 2020. doi: 10.1126/science.aaz2856.

A. Antonova et al. *A&A*, 487(1):317–322, Aug. 2008. doi: 10.1051/0004-6361:20079275.

É. Artigau, S. Bouchard, R. Doyon, and D. Lafrenière. *ApJ*, 701(2):1534–1539, Aug. 2009. doi: 10.1088/0004-637X/701/2/1534.

R. Ashtari, A. Sciola, J. D. Turner, and K. Stevenson. *ApJ*, 939(1):24, Nov. 2022. doi: 10.3847/1538-4357/ac92f5.

S. V. Badman et al. *Space Sci. Rev.*, 187(1-4):99–179, Apr. 2015. doi: 10.1007/s11214-014-0042-x.

F. Bagenal. Planetary Magnetospheres. In T. D. Oswalt, L. M. French, and P. Kalas, editors, *Planets, Stars and Stellar Systems. Volume 3: Solar and Stellar Planetary Systems*, page 251. Springer, 2013. doi: 10.1007/978-94-007-5606-9_6.

D. C. Bardalez Gagliuffi et al. *ApJ*, 883(2):205, Oct. 2019. doi: 10.3847/1538-4357/ab253d.

A. C. Barr, V. Dobos, and L. L. Kiss. *A&A*, 613:A37, May 2018. doi: 10.1051/0004-6361/201731992.

T. S. Bastian, W. D. Cotton, and G. Hallinan. *ApJ*, 935(2):99, Aug. 2022. doi: 10.3847/1538-4357/ac7d57.

L. Ben-Jaffel et al. *Nature Astronomy*, 6:141–153, Jan. 2022. doi: 10.1038/s41550-021-01505-x.

G. F. Benedict et al. *AJ*, 152(5):141, Nov. 2016. doi: 10.3847/0004-6256/152/5/141.

E. Berger. *ApJ*, 572(1):503–513, June 2002. doi: 10.1086/340301.

E. Berger. *ApJ*, 648(1):629–636, Sept. 2006. doi: 10.1086/505787.

E. Berger et al. *Nature*, 410(6826):338–340, Mar. 2001. doi: 10.1038/35066514.

E. Berger et al. *ApJ*, 695(1):310–316, Apr. 2009. doi: 10.1088/0004-637X/695/1/310.

W. M. J. Best et al. *ApJ*, 967(2):115, June 2024. doi: 10.3847/1538-4357/ad39ef.

E. G. Blackman and J. A. Tarduno. *MNRAS*, 481(4):5146–5155, Dec. 2018. doi: 10.1093/mnras/sty2640.

C. H. Blaske and J. G. O'Rourke. *Journal of Geophysical Research (Planets)*, 126(7):e06739, July 2021. doi: 10.1029/2020JE00673910.1002/essoar.10509905.1.

S. Bloot et al. *A&A*, 682:A170, Feb. 2024. doi: 10.1051/0004-6361/202348065.

S. J. Bolton et al. *Nature*, 415(6875):987–991, Feb. 2002. doi: 10.1038/415987a.

I. Bonati, M. Lasbleis, and L. Noack. *Journal of Geophysical Research (Planets)*, 126(5):e06724, May 2021. doi: 10.1029/2020JE00672410.1002/essoar.10504524.1.

B. Bonfond, Z. Yao, and D. Grodent. *Journal of Geophysical Research (Space Physics)*, 125(11): e28152, Nov. 2020. doi: 10.1029/2020JA028152.

D. A. Brain, M. M. Kao, and J. G. O'Rourke. *arXiv e-prints*, art. arXiv:2404.15429, Apr. 2024. doi: 10.48550/arXiv.2404.15429.

R. Braun et al. *arXiv e-prints*, art. arXiv:1912.12699, Dec. 2019. doi: 10.48550/arXiv.1912.12699.

A. J. Burgasser and M. E. Putman. *ApJ*, 626(1):486–497, June 2005. doi: 10.1086/429788.

J. O. Burns et al. *Planet. Sci. J.*, 2(2):44, Apr. 2021. doi: 10.3847/PSJ/abdfc3.

J. R. Callingham et al. *Nature Astronomy*, 5:1233–1239, Dec. 2021. doi: 10.1038/s41550-021-01483-0.

J. R. Callingham et al. *A&A*, 670:A124, Feb. 2023. doi: 10.1051/0004-6361/202245567.

J. R. Callingham et al. *Nature Astronomy*, 8:1359–1372, Nov. 2024. doi: 10.1038/s41550-024-02405-6.

S. Carolan et al. *MNRAS*, 508(4):6001–6012, Dec. 2021. doi: 10.1093/mnras/stab2947.

G. Chabrier, I. Baraffe, M. Phillips, and F. Debras. *A&A*, 671:A119, Mar. 2023. doi: 10.1051/0004-6361/202243832.

U. R. Christensen, V. Holzwarth, and A. Reiners. *Nature*, 457(7226):167–169, Jan. 2009. doi: 10.1038/nature07626.

J. B. Climent et al. *Science*, 381(6662):1120–1124, Sept. 2023. doi: 10.1126/science.adg6635.

O. Cohen. *MNRAS*, 417(4):2592–2600, Nov. 2011. doi: 10.1111/j.1365-2966.2011.19428.x.

B. Collet et al. *Journal of Geophysical Research (Space Physics)*, 129(5):e2024JA032422, May 2024. doi: 10.1029/2024JA032422.

B. Collet et al. *Geophysical Research Letters*, 52(9):e2024GL114447, 2025. doi: https://doi.org/10.1029/2024GL114447. URL https://agupubs.onlinelibrary.wiley.com/doi/abs/10.1029/2024GL114447. e2024GL114447 2024GL114447.

C. M. Cordun, H. K. Vedantham, M. A. Brentjens, and F. F. S. van der Tak. *A&A*, 693:A162, Jan. 2025. doi: 10.1051/0004-6361/202452868.

S. W. H. Cowley and E. J. Bunce. *Planet. Space Sci.*, 49(10-11):1067–1088, Aug. 2001. doi: 10.1016/S0032-0633(00)00167-7.

S. Curiel, G. N. Ortiz-León, A. J. Mioduszewski, and R. M. Torres. *AJ*, 160(3):97, Sept. 2020. doi: 10.3847/1538-3881/ab9e6e.

S. Curiel, G. N. Ortiz-León, A. J. Mioduszewski, and J. Sanchez-Bermudez. *AJ*, 164(3):93, Sept. 2022. doi: 10.3847/1538-3881/ac7c66.

S. Curiel, G. N. Ortiz-León, A. J. Mioduszewski, and A. B. Arenas-Martinez. *ApJ*, 967(2):112, June 2024. doi: 10.3847/1538-4357/ad3df6.

S. Daley-Yates and I. R. Stevens. *MNRAS*, 479(1):1194–1209, Sept. 2018. doi: 10.1093/mnras/sty1652.

C. E. Davis et al. *ApJ*, 994(2):198, Dec. 2025. doi: 10.3847/1538-4357/ae1015.

I. de Pater. *J. Geophys. Res.*, 86(A5):3397–3422, May 1981. doi: 10.1029/JA086iA05p03397.

M. D. Desch and M. L. Kaiser. *Nature*, 310(5980):755–757, Aug. 1984. doi: 10.1038/310755a0.

C. Dong, Z. Huang, and M. Lingam. *ApJL*, 882(2):L16, Sept. 2019. doi: 10.3847/2041-8213/ab372c.

L. N. Driessen et al. *PASA*, 41:e084, Nov. 2024. doi: 10.1017/pasa.2024.72.

S. Dulaimi, A. Golden, R. P. Boyle, and R. F. Butler. *MNRAS*, 518(3):4428–4437, Jan. 2023. doi: 10.1093/mnras/stac2894.

J. W. Dungey. *J. Geophys. Res.*, 66(4):1043–1047, Apr. 1961. doi: 10.1029/JZ066i004p01043.

Z. Eker, F. Soydugan, and S. Bilir. *Physics and Astronomy Reports*, 2(1):41–57, June 2024. doi: 10.26650/PAR.2024.00001.

K. El-Badry et al. *The Open Journal of Astrophysics*, 7:100, Nov. 2024. doi: 10.33232/001c.125461.

F. Elekes and J. Saur. *A&A*, 671:A133, Mar. 2023. doi: 10.1051/0004-6361/202244947.

N. Espinoza et al. *ApJL*, 990(2):L52, Sept. 2025. doi: 10.3847/2041-8213/adf42e.

J. K. Faherty et al. *Nature*, 628(8008):511–514, Apr. 2024. doi: 10.1038/s41586-024-07190-w.

J. Forbrich, E. Berger, and M. J. Reid. *ApJ*, 777(1):70, Nov. 2013. doi: 10.1088/0004-637X/777/

1/70.
J. Forbrich et al. *ApJ*, 827(1):22, Aug. 2016. doi: 10.3847/0004-637X/827/1/22.
Y. Fujii et al. *ApJ*, 820(2):122, Apr. 2016. doi: 10.3847/0004-637X/820/2/122.
B. J. Fulton and E. A. Petigura. *AJ*, 156(6):264, Dec. 2018. doi: 10.3847/1538-3881/aae828.
Gaia Collaboration et al. *A&A*, 674:A1, June 2023. doi: 10.1051/0004-6361/202243940.
J. N. Girard et al. *A&A*, 587:A3, Mar. 2016. doi: 10.1051/0004-6361/201527518.
J. E. Gizis et al. *ApJ*, 779(2):172, Dec. 2013. doi: 10.1088/0004-637X/779/2/172.
J. E. Gizis et al. *AJ*, 152(5):123, Nov. 2016. doi: 10.3847/0004-6256/152/5/123.
J.-M. Grießmeier et al. *A&A*, 425:753–762, Oct. 2004. doi: 10.1051/0004-6361:20035684.
J. M. Grießmeier, P. Zarka, and H. Spreeuw. *A&A*, 475(1):359–368, Nov. 2007. doi: 10.1051/0004-6361:20077397.
J. C. Guirado et al. *ApJ*, 987(1):7, July 2025. doi: 10.3847/1538-4357/add5f3.
G. Hallinan et al. *ApJL*, 663(1):L25–L28, July 2007. doi: 10.1086/519790.
G. Hallinan et al. *ApJ*, 684(1):644–653, Sept. 2008. doi: 10.1086/590360.
G. Hallinan et al. *ApJ*, 762(1):34, Jan. 2013. doi: 10.1088/0004-637X/762/1/34.
G. Hallinan, S. P. Littlefair, G. Cotter, and et al. *Nature*, 523:568–571, 2015. doi: 10.1038/nature14619.
L. K. Harding et al. *ApJ*, 779(2):101, Dec. 2013. doi: 10.1088/0004-637X/779/2/101.
A. Hegedus et al. *Radio Science*, 55(2):e06891, Feb. 2020. doi: 10.1029/2019RS006891.
R. Heller and M. Hippke. *Nature Astronomy*, 8:193–206, Feb. 2024. doi: 10.1038/s41550-023-02148-w.
C. Helling, M. Jardine, and F. Mokler. *ApJ*, 737(1):38, Aug. 2011. doi: 10.1088/0004-637X/737/1/38.
S. Hess, B. Cecconi, and P. Zarka. , 35(13):L13107, July 2008. doi: 10.1029/2008GL033656.
S. L. G. Hess and P. Zarka. *A&A*, 531:A29, July 2011. doi: 10.1051/0004-6361/201116510.
T. W. Hill. *J. Geophys. Res.*, 106(A5):8101–8108, May 2001. doi: 10.1029/2000JA000302.
M. Jardine and A. Collier Cameron. *MNRAS*, 482(3):2853–2860, Jan. 2019. doi: 10.1093/mnras/sty2872.
M. L. Kaiser, M. D. Desch, J. W. Warwick, and J. B. Pearce. *Science*, 209(4462):1238–1240, Sept. 1980. doi: 10.1126/science.209.4462.1238.
M. M. Kao and J. S. Pineda. *Monthly Notices of the Royal Astronomical Society*, 539(3):2292–2306, May 2025. doi: 10.1093/mnras/stae905.
M. M. Kao and E. L. Shkolnik. *Monthly Notices of the Royal Astronomical Society*, 527(3):6835–6866, January 2024. doi: 10.1093/mnras/stad2272.
M. M. Kao et al. *ApJ*, 818(1):24, Feb. 2016. doi: 10.3847/0004-637X/818/1/24.
M. M. Kao, G. Hallinan, J. S. Pineda, and D. J. Stevenson. *The Astrophysical Journal Supplement Series*, 237(2):25, 2018. doi: 10.3847/1538-4365/aac2d5.
M. M. Kao, A. J. Mioduszewski, J. Villadsen, and et al. *Nature*, 619:272–275, 2023. doi: 10.1038/s41586-023-06138-w.
R. D. Kavanagh and H. K. Vedantham. *MNRAS*, 524(4):6267–6284, Oct. 2023. doi: 10.1093/mnras/stad2035.
R. D. Kavanagh and A. A. Vidotto. *MNRAS*, 493(1):1492–1497, Mar. 2020. doi: 10.1093/mnras/staa422.

R. D. Kavanagh et al. *MNRAS*, 485(4):4529–4538, June 2019. doi: 10.1093/mnras/stz655.

R. D. Kavanagh et al. *MNRAS*, 504(1):1511–1518, June 2021. doi: 10.1093/mnras/stab929.

R. D. Kavanagh et al. *MNRAS*, 514(1):675–688, July 2022. doi: 10.1093/mnras/stac1264.

R. D. Kavanagh, H. K. Vedantham, K. Rose, and S. Bloot. *A&A*, 692:A66, Dec. 2024. doi: 10.1051/0004-6361/202452094.

K. Kilmetis, A. A. Vidotto, A. Allan, and D. Kubyshkina. *MNRAS*, 535(4):3646–3655, Dec. 2024. doi: 10.1093/mnras/stae2505.

D. Kipping et al. *Nature Astronomy*, 9:795–798, June 2025. doi: 10.1038/s41550-025-02547-1.

K. G. Kislyakova et al. *A&A*, 677:A109, Sept. 2023. doi: 10.1051/0004-6361/202245225.

B. Klein et al. *MNRAS*, 502(1):188–205, Mar. 2021. doi: 10.1093/mnras/staa3702.

M. Knapp, L. Paritsky, E. Kononov, and M. M. Kao. *arXiv e-prints*, art. arXiv:2404.08432, Apr. 2024. doi: 10.48550/arXiv.2404.08432.

P. Kollmann et al. , 49(23):e2022GL098474, Dec. 2022. doi: 10.1029/2022GL098474.

A. A. Kuznetsov et al. *ApJ*, 746(1):99, Feb. 2012. doi: 10.1088/0004-637X/746/1/99.

L. Lamy. *Philosophical Transactions of the Royal Society of London Series A*, 378(2187):20190481, Dec. 2020. doi: 10.1098/rsta.2019.0481.

L. Lamy et al. *Journal of Geophysical Research (Space Physics)*, 113(A10):A10213, Oct. 2008a. doi: 10.1029/2008JA013464.

L. Lamy et al. *Journal of Geophysical Research (Space Physics)*, 113(A7):A07201, July 2008b. doi: 10.1029/2007JA012900.

L. Lamy et al. , 37(12):L12104, June 2010. doi: 10.1029/2010GL043415.

L. Lamy, L. Colomban, and P. Zarka. In *European Planetary Science Congress*, pages EPSC2021–707, Sept. 2021. doi: 10.5194/epsc2021-707.

L. Lamy, J. E. Waters, and C. K. Louis. In C. K. Louis et al., editors, *Planetary, Solar and Heliospheric Radio Emissions IX*, page 103091, Jan. 2023. doi: 10.25546/103091.

T. J. W. Lazio and W. M. Farrell. *ApJ*, 668(2):1182–1188, Oct. 2007. doi: 10.1086/519730.

T. J. W. Lazio et al. *AJ*, 139(1):96–101, Jan. 2010. doi: 10.1088/0004-6256/139/1/96.

P. Leto et al. *MNRAS*, 459(2):1159–1169, June 2016. doi: 10.1093/mnras/stw639.

P. Leto et al. *MNRAS*, 507(2):1979–1998, Oct. 2021. doi: 10.1093/mnras/stab2168.

B. Liu et al. *A&A*, 638:A88, June 2020. doi: 10.1051/0004-6361/202037720.

M. S. Longair. *High Energy Astrophysics*. Cambridge University Press, Cambridge, United Kingdom, 3rd edition, 2011.

P. Louarn et al. *J. Geophys. Res.*, 95(A5):5983–5995, May 1990. doi: 10.1029/JA095iA05p05983.

C. K. Louis et al. *A&A*, 627:A30, July 2019. doi: 10.1051/0004-6361/201935161.

K. L. Luhman. *ApJL*, 767(1):L1, Apr. 2013. doi: 10.1088/2041-8205/767/1/L1.

A. T. Lukashenko, A. S. Lavrukhin, I. I. Alexeev, and E. S. Belenkaya. *Astronomy Letters*, 46(11): 762–773, Nov. 2020. doi: 10.1134/S1063773720110043.

C. Lynch, R. L. Mutel, and M. Güdel. *ApJ*, 802(2):106, Apr. 2015. doi: 10.1088/0004-637X/802/2/106.

C. R. Lynch, T. Murphy, E. Lenc, and D. L. Kaplan. *MNRAS*, 478(2):1763–1775, Aug. 2018. doi: 10.1093/mnras/sty1138.

E. Magaudda et al. *A&A*, 687:A95, July 2024. doi: 10.1051/0004-6361/202449403.

G. Marc, A. Sicard, Q. Nénon, and R. Belmont. *Journal of Geophysical Research (Space Physics)*, 129(10):e2024JA032563, Oct. 2024. doi: 10.1029/2024JA032563.

M. S. Marques et al. *A&A*, 604:A17, Aug. 2017. doi: 10.1051/0004-6361/201630025.

K. Matuszewska et al. *PASP*, 134(1038):084401, Aug. 2022. doi: 10.1088/1538-3873/ac6a7a.

E. Mauduit, J.-M. Grießmeier, P. Zarka, and J. D. Turner. In C. K. Louis et al., editors, *Planetary, Solar and Heliospheric Radio Emissions IX*, page 103092, Jan. 2023. doi: 10.25546/103092.

B. H. Mauk and N. J. Fox. *Journal of Geophysical Research (Space Physics)*, 115(A12):A12220, Dec. 2010. doi: 10.1029/2010JA015660.

M. McLean et al. *ApJ*, 741(1):27, Nov. 2011. doi: 10.1088/0004-637X/741/1/27.

S. A. Metchev et al. *ApJ*, 799(2):154, Feb. 2015. doi: 10.1088/0004-637X/799/2/154.

P. A. Miles-Páez, S. A. Metchev, and B. George. *MNRAS*, 521(1):952–968, May 2023. doi: 10.1093/mnras/stad273.

T. Murphy et al. *MNRAS*, 446(3):2560–2565, Jan. 2015. doi: 10.1093/mnras/stu2253.

J. D. Nichols. *MNRAS*, 414(3):2125–2138, July 2011. doi: 10.1111/j.1365-2966.2011.18528.x.

A. Oklopčić, M. Silva, P. Montero-Camacho, and C. M. Hirata. *ApJ*, 890(1):88, Feb. 2020. doi: 10.3847/1538-4357/ab67c6.

J. E. Owen and F. C. Adams. *MNRAS*, 444(4):3761–3779, Nov. 2014. doi: 10.1093/mnras/stu1684.

A. Palau et al. *New Astron. Rev.*, 99:101711, Dec. 2024. doi: 10.1016/j.newar.2024.101711.

L. Parc et al. *A&A*, 688:A59, Aug. 2024. doi: 10.1051/0004-6361/202449911.

E. N. Parker. *ApJ*, 128:664, Nov. 1958. doi: 10.1086/146579.

R. R. Paudel et al. *MNRAS*, 494(4):5751–5760, June 2020. doi: 10.1093/mnras/staa1137.

N. Phan-Bao et al. *ApJ*, 658(1):553–556, Mar. 2007. doi: 10.1086/511061.

J. S. Pineda, G. Hallinan, and M. M. Kao. *Astrophysical Journal*, 846:75, 2017. doi: 10.3847/1538-4357/aa8459.

M. Popinchalk et al. *ApJ*, 916(2):77, Aug. 2021. doi: 10.3847/1538-4357/ac0444.

J. Radigan. *ApJ*, 797(2):120, Dec. 2014. doi: 10.1088/0004-637X/797/2/120.

A. Reiners and U. R. Christensen. *A&A*, 522:A13, Nov. 2010. doi: 10.1051/0004-6361/201014251.

T. Richey-Yowell et al. *ApJ*, 903(1):74, Nov. 2020. doi: 10.3847/1538-4357/abb826.

M. J. Rioja and R. Dodson. *A&ARv*, 28(1):6, Sept. 2020. doi: 10.1007/s00159-020-00126-z.

J. Robrade and J. H. M. M. Schmitt. *A&A*, 497(2):511–520, Apr. 2009. doi: 10.1051/0004-6361/200811348.

K. Rose et al. *ApJL*, 951(2):L43, July 2023. doi: 10.3847/2041-8213/ace188.

E. Roussos et al. *Planet. Space Sci.*, 104:3–17, Dec. 2014. doi: 10.1016/j.pss.2014.03.021.

M. Route. *ApJ*, 845(1):66, Aug. 2017. doi: 10.3847/1538-4357/aa7ede.

M. Route and A. Wolszczan. *ApJL*, 747(2):L22, Mar. 2012. doi: 10.1088/2041-8205/747/2/L22.

M. Route and A. Wolszczan. *ApJL*, 821(2):L21, Apr. 2016a. doi: 10.3847/2041-8205/821/2/L21.

M. Route and A. Wolszczan. *ApJ*, 830(2):85, Oct. 2016b. doi: 10.3847/0004-637X/830/2/85.

G. B. Rybicki and A. P. Lightman. *Radiative Processes in Astrophysics*. Wiley-VCH, Weinheim, Germany, 1st edition, 1986.

J. Saur et al. *A&A*, 552:A119, Apr. 2013. doi: 10.1051/0004-6361/201118179.

J. Saur et al. *A&A*, 655:A75, Nov. 2021. doi: 10.1051/0004-6361/202040230.

M. Schlecker et al. *A&A*, 664:A180, Aug. 2022. doi: 10.1051/0004-6361/202142543.

T. W. Shimwell et al. *A&A*, 659:A1, Mar. 2022. doi: 10.1051/0004-6361/202142484.

M. Shoda, S. R. Cranmer, and S. Toriumi. *ApJ*, 957(2):71, Nov. 2023. doi: 10.3847/1538-4357/

acfa72.

A. P. Showman, X. Tan, and V. Parmentier. *Space Sci. Rev.*, 216(8):139, Dec. 2020. doi: 10.1007/s11214-020-00758-8.

G. Sicorello et al. *A&A*, 703:A69, Nov. 2025. doi: 10.1051/0004-6361/202556176.

A. M. S. Smith et al. *MNRAS*, 395(1):335–341, May 2009. doi: 10.1111/j.1365-2966.2009.14510.x.

C. L. Smith, M. Moe, and K. M. Kratter. *ApJ*, 975(1):153, Nov. 2024. doi: 10.3847/1538-4357/ad6dd2.

E. Solano et al. *MNRAS*, 501(1):281–290, Jan. 2021. doi: 10.1093/mnras/staa3423.

S. Stanley and J. Bloxham. *Nature*, 428(6979):151–153, Mar. 2004. doi: 10.1038/nature02376.

G. Stefánsson et al. *Science*, 382(6674):1031–1035, Dec. 2023. doi: 10.1126/science.abo0233.

C. Tasse et al. *Nature Astronomy*, 10:410–419, Mar. 2026. doi: 10.1038/s41550-025-02757-7.

R. A. Treumann. *A&ARv*, 13(4):229–315, Aug. 2006. doi: 10.1007/s00159-006-0001-y.

J. D. Turner et al. *A&A*, 645:A59, Jan. 2021. doi: 10.1051/0004-6361/201937201.

E. A. van Dijk and Y. Miguel. *MNRAS*, 540(2):1544–1559, June 2025. doi: 10.1093/mnras/staf814.

H. Vedantham et al. In *Advancing Astrophysics with the SKA – II (AASKAII)*. 2026. arXiv search: Report number AASKAII/Vedantham01.

H. K. Vedantham et al. *Nature Astronomy*, 4:577–583, Feb. 2020. doi: 10.1038/s41550-020-1011-9.

H. K. Vedantham et al. *A&A*, 675:L6, July 2023. doi: 10.1051/0004-6361/202244965.

T. Velusamy et al. *PASP*, 132(1016):104402, Oct. 2020. doi: 10.1088/1538-3873/aba69e.

A. A. Vidotto and J. F. Donati. *A&A*, 602:A39, June 2017. doi: 10.1051/0004-6361/201629700.

A. A. Vidotto et al. *MNRAS*, 423(4):3285–3298, July 2012. doi: 10.1111/j.1365-2966.2012.21122.x.

G.-H. Voigt. *Handbook of Atmospheric Electrodynamics*, volume 2. CRC Press, 1995.

J. M. Vos, K. N. Allers, and B. A. Biller. *ApJ*, 842(2):78, June 2017. doi: 10.3847/1538-4357/aa73cf.

J. M. Vos et al. *ApJ*, 944(2):138, Feb. 2023. doi: 10.3847/1538-4357/acab58.

Y.-F. Wang et al. *A&A*, 660:A38, Apr. 2022. doi: 10.1051/0004-6361/202142009.

M. L. Waskom. *Journal of Open Source Software*, 6(60):3021, 2021. doi: 10.21105/joss.03021. URL https://doi.org/10.21105/joss.03021.

C. Weber et al. *MNRAS*, 480(3):3680–3688, Nov. 2018. doi: 10.1093/mnras/sty2079.

E. J. Weber and L. Davis, Jr. *ApJ*, 148:217–227, Apr. 1967. doi: 10.1086/149138.

P. K. G. Williams. Radio Emission from Ultracool Dwarfs. In H. J. Deeg and J. A. Belmonte, editors, *Handbook of Exoplanets*, page 171. 2018. doi: 10.1007/978-3-319-55333-7_171.

P. K. G. Williams and E. Berger. *ApJ*, 808(2):189, Aug. 2015. doi: 10.1088/0004-637X/808/2/189.

P. K. G. Williams et al. *ApJ*, 799(2):192, Feb. 2015a. doi: 10.1088/0004-637X/799/2/192.

P. K. G. Williams et al. *ApJ*, 815(1):64, Dec. 2015b. doi: 10.1088/0004-637X/815/1/64.

P. K. G. Williams, J. E. Gizis, and E. Berger. *ApJ*, 834(2):117, Jan. 2017. doi: 10.3847/1538-4357/834/2/117.

H. N. Williamson et al. , 53(2):e2025GL119589, Jan. 2026. doi: 10.1029/2025GL119589.

B. E. Wood et al. *ApJ*, 915(1):37, July 2021. doi: 10.3847/1538-4357/abfda5.

C. S. Wu and L. C. Lee. *ApJ*, 230:621–626, June 1979. doi: 10.1086/157120.

R. K. Yadav and D. P. Thorngren. *ApJL*, 849(1):L12, Nov. 2017. doi: 10.3847/2041-8213/aa93fd.

Z. H. Yao et al. *Journal of Geophysical Research (Space Physics)*, 127(10):e2021JA029894, Oct.

2022. doi: 10.1029/2021JA029894.

T. W. H. Yiu, H. K. Vedantham, J. R. Callingham, and T. W. Shimwell. *A&A*, 704:A281, Dec. 2025. doi: 10.1051/0004-6361/202554844.

M. Zaghoo and G. W. Collins. *ApJ*, 862(1):19, July 2018. doi: 10.3847/1538-4357/aac6e8.

P. Zarka. *Journal of Geophysical Research*, 103:20159–20194, 1998. doi: 10.1029/98JE01323.

P. Zarka. *Advances in Space Research*, 33(11):2045–2060, Jan. 2004. doi: 10.1016/j.asr.2003.07.055.

P. Zarka. *Planet. Space Sci.*, 55(5):598–617, Apr. 2007. doi: 10.1016/j.pss.2006.05.045.

P. Zarka. *Star-Planet Interactions in the Radio Domain: Prospect for Their Detection*, pages 1–19. Springer Nature Switzerland, Cham, 2025. ISBN 978-3-319-30648-3. doi: 10.1007/978-3-319-30648-3_22-3. URL https://doi.org/10.1007/978-3-319-30648-3_22-3.

P. Zarka et al. In H. O. Rucker, S. J. Bauer, and A. Lecacheux, editors, *Planetary Radio Emission IV*, pages 101–127, Jan. 1997.

P. Zarka, R. A. Treumann, B. P. Ryabov, and V. B. Ryabov. *Astro. & Space Sci.*, 277:293–300, June 2001. doi: 10.1023/A:1012221527425.

P. Zarka, B. Cecconi, and W. S. Kurth. *Journal of Geophysical Research (Space Physics)*, 109(A9): A09S15, Sept. 2004. doi: 10.1029/2003JA010260.

P. Zarka et al. *A&A*, 618:A84, Oct. 2018. doi: 10.1051/0004-6361/201833586.

P. Zarka et al. *Journal of Geophysical Research (Space Physics)*, 126(10):e29780, Oct. 2021. doi: 10.1029/2021JA02978010.1002/essoar.10507542.1.

P. Zarka et al. *A&A*, 695:A95, Mar. 2025. doi: 10.1051/0004-6361/202450950.

Q. Zhang et al. *ApJ*, 897(1):11, July 2020. doi: 10.3847/1538-4357/ab9177.

X. Zhang et al. *A&A*, 700:A140, Aug. 2025. doi: 10.1051/0004-6361/202555209.

A. Zic et al. *MNRAS*, 483(1):614–623, Feb. 2019. doi: 10.1093/mnras/sty3163.